國立臺灣大學電機資訊學院光電工程學研究所

碩士論文

Graduate Institute of Photonics and Optoelectronics

College of Electrical Engineering and Computer Science

National Taiwan University

Master Thesis

合成在特定波長有表面電漿共振之金屬奈米結構

Synthesis of Metallic Nanostructures with Surface-Plasmon

Resonance at Designated Wavelengths

歐陽良昱

Liang-Yu Ou Yang

指導教授：江衍偉 博士

中華民國98年7月

July 2009

國立臺灣大學碩士學位論文
口試委員會審定書

合成在特定波長有表面電漿共振之金屬奈米結構
Synthesis of Metallic Nanostructures with
Surface-Plasmon Resonance at Designated
Wavelengths

本論文係歐陽良昱君（學號 R96941009）在國立臺灣大學光電工程學研究所完成之碩士學位論文，於民國 98 年 7 月 21 日承下列考試委員審查通過及口試及格，特此證明

口試委員：

江衍伯 （指導教授）

楊志忠　張宏鋼

吳育任

所長　黃升龍

誌　謝

『桃李春風一杯酒，江湖夜雨十年燈』，碩士兩年，首先感謝江衍偉老師的耐心指導，不論是在研究方面或電磁學，都讓我收穫良多。老師對於學問的純真追求，堪稱典範，跟江老師討論電磁問題，是我在碩士生涯中最快樂的時光。另外也感謝張宏鈞、吳育任、楊志忠老師對論文提出寶貴意見。接著要感謝我的父母，他們是我人生中最重要的人，有他們在經濟與心靈上的支持，讓我有勇氣去面對任何難題。也感謝郭仰、王志洋、蔡富吉、莊文宏、林俊安、陳弘履、沈昌煒等學長在理論與程式上的幫助，讓我的研究能順利完成。方嘉鵬、吳碩彥同學則是在學習、玩樂、修課、聯誼上不可多得的好夥伴，而于贊堯、廖家鴻、張然凱學弟的加入，對實驗室又注入了一份熱情與活力。最後，要感謝禎禧，在這兩年裡默默的陪伴著我。

歐陽良昱　謹識

予台大光電工程研究所

民國九十八年七月

摘要

我們利用模擬退火法與邊界積分方程法來合成在特定波長具有表面電漿共振特性的金屬奈米結構。數值結果依應用可分為：藍光 LED（波長 435 nm）、白光 LED（波長 450 nm 與 570 nm）、與綠光 LED（波長 535 nm）。藍光 LED 係由二金屬圓柱部分嵌於金屬半空間之奈米結構所組成。吾人首先合成一結構，其表面電漿極化子和局域表面電漿子在單一波長（435 nm）能有效耦合。接著再合成另一結構，使其在另一波長（520 nm）僅有局域表面電漿子之共振。數值模擬顯示：表面電漿極化子和局域表面電漿子在單一波長有效耦合時，確實可提升其附近電偶極之輻射量。白光 LED 係由二分離之金屬圓柱與一金屬半空間之奈米結構所組成。吾人合成一結構，在藍光波長（450 nm）與黃光波長（570 nm）皆具有局域表面電漿子共振，因而提升混光而成的白光發光量。綠光 LED 係由二分離之金屬橢圓柱與一金屬半空間之奈米結構所組成。吾人合成一結構，其表面電漿極化子和局域表面電漿子在單一波長（535 nm）能有效耦合，因而提升電偶極之輻射量與輻射效率。

Abstract

The simulated annealing and the boundary integral-equation methods are used to synthesize metallic nanostructures with surface-plasmon resonance properties at designated wavelengths. The numerical results include three parts according to the possible applications: blue-light LEDs (wavelength 435 nm), white-light LEDs (wavelengths 450 nm and 570 nm), and green-light LEDs (wavelength 535 nm). For the blue-light LEDs, the structure consists of two metallic circular cylinders partially embedded in a metallic half-space. We first synthesize a metallic nanostructure such that the surface plasmon polariton (SPP) and the localized surface plasmon (LSP) couple effectively at their common resonant wavelength (435 nm). Next, we synthesize another structure for optimization at wavelength 520 nm, at which only the LSP resonance occurs. From numerical simulations, it is demonstrated that the enhancement of the dipole emission is better for optimization at wavelength 435 nm than that at wavelength 520 nm. In the aspect of white-light LEDs, the structure is composed of two separate metallic circular cylinders and a metallic half-space. We synthesize a

metallic nanostructure, which has LSP resonances at wavelength 450 nm (blue light) and at wavelength 570 nm (yellow light), leading to the enhancement of white-light emission. For the green-light LEDs, the structure consists of two separate metallic elliptical cylinders and a metallic half-space. We synthesize a metallic nanostructure such that the SPP and LSP couple effectively at their common resonant wavelength (535 nm), leading to the enhancement of both the dipole emission and the emission efficiency.

Table of Contents

List of Figures

VII

List of Tables

Chapter 1
Introduction

The phenomenon of surface plasmon (SP) has been explored since the beginning of last century. The SP represents the behavior which electrons collectively oscillate near the surface of metal. For the applications of SP in the optical field and nanophotonics, the devices using SP in sub-wavelength scale enable us to miniaturize integrated optical circuits for confining or controlling electromagnetic wave. SP waveguides are typical examples. In chemical areas, the SP can be applied to enhance the intensity of signal for Raman scattering. This technique is called "surface enhanced Raman spectroscopy (SERS)". In biological areas, the idea of SP field enhancement is used to construct the biosensors for detecting interesting molecules with high sensitivity. In recent years, the coupling of SP with a light emitter for enhancing the emission efficiency has been widely studied [1-18]. The reason for emission enhancement can be explained by the classical electrodynamics. If the SP mode has a large field value in the neighborhood of a dipole, the radiation of that dipole will be enhanced [19]. It means the enhancement

of spontaneous emission rate through the coupling between quantum wells and SP is possible. Hence, the SP-assisted devices to improve light extraction efficiency and internal quantum efficiency have become attractive. Many approaches have been proposed to enhance the light extraction efficiency, such as LEDs with resonant cavity, surface texturing, and output coupling surface plasmon at corrugated or grating metallic surfaces.

In general, the SP modes can be classified as the surface plasmon polariton (SPP) and localized surface plasmon (LSP). In this thesis, we focus on discussing the coupling properties of both SPP and LSP. The coupling of SPP and LSP are numerically investigated in the frequency domain. The organization of this thesis is outlined as follows.

In chapter 2, the fundamentals of the SP are briefly reviewed. In chapter 3, we introduce our simulation methods, including boundary integral-equation method (BIEM) and simulated annealing (SA) technique. Compared to the commonly used finite-difference time-domain (FDTD) method, the BIEM can deal with complex geometries easier than FDTD. The reason is that FDTD is a formulation using fixed square space grids, but BIEM is with unstructured-mesh

based on a surface formulation, which automatically takes care of discontinuities between materials and models arbitrarily shaped structures. The SA is a probabilistic and iterative method of optimization mimicking the real annealing process of matter [20, 21]. We also introduce the theory of SA and its application to synthesizing metallic nanostructures in this chapter. In chapter 4, the numerical simulation results are presented. Finally, some conclusions are drawn in chapter 5.

Chapter 2
Surface Plasmon (SP)

2.1 Surface plasmon polariton (SPP)

A plasma is a quasi-neutral gas of the electrons, positive ions, and neutral particles possessing certain collective behaviors. The tendency to restore the charge neutrality leads to the plasma oscillation with an angular frequency ω_p given by

$$\omega_p = \sqrt{\frac{Ne^2}{m_e \varepsilon_0}}, \qquad (2.1)$$

where N is the number density of electrons, m_e is the mass of an electron, ε_0 is the permittivity in free space, and e is the electric charge of an electron.

A noble metal, such as Ag or Au, can be regarded as a cold plasma. In other words, we can consider it as a dielectric with an effective dielectric constant given by the Drude model [22]

$$\varepsilon_m(\omega) = 1 - \frac{\omega_p^2}{\omega(\omega + i\gamma)}, \qquad (2.2)$$

where γ is the damping constant or collision frequency. In this study, the dielectric constant of Ag is assumed to follow the Drude model with the angular plasma frequency at $\omega_p = 1.19 \times 10^{16}$ (rad·s^{-1}) and the damping

constant at $\gamma = 1.32 \times 10^{14}$ (rad·s^{-1}). For another metal Au, $\omega_p = 9.37 \times 10^{15}$ (rad·s^{-1}) and $\gamma = 1.04 \times 10^{14}$ (rad·s^{-1}).

In the bulk of a cold plasma, the plasma oscillation can be described as an oscillatory fluctuation of the electron density. On the other aspect, there is another mode distinct from the bulk plasma mode, known as "surface plasmon". It can exist on the interface between a metal and a dielectric, and is associated with the oscillation of surface charges excited by exterior electromagnetic field. Note that the electromagnetic field and polarization wave can be quantized with energy quanta called polaritons. Hence, a combination of excitation of surface plasmon and polariton is called the surface plasmon polariton (SPP). A SPP is evanescent perpendicular to the metal-dielectric interface. This nonradiative surface wave can be analyzed by solving Maxwell's equations and matching the associated boundary conditions.

Figure 2.1 shows the interaction between the electromagnetic wave and the surface plasma oscillation at a metal-dielectric flat interface. In the figure, we consider the p-polarized (or TM) wave with the electric field lying in the plane of incidence. It can be shown that the x-component wavevector of SPP is given by [23]

$$k_{SPP} = \frac{\omega}{c} \sqrt{\frac{\varepsilon_m(\omega)\varepsilon_d}{\varepsilon_m(\omega) + \varepsilon_d}} . \tag{2.3}$$

Here, $\varepsilon_m(\omega)$ is the frequency-dependent dielectric constant of the metal and ε_d is the dielectric constant of the dielectric.

For the lossless Drude model, k_{SPP} approaches infinity as ω tends to the SPP resonant frequency

$$\omega_{SPP} = \frac{\omega_p}{\sqrt{1 + \varepsilon_d}} . \tag{2.4}$$

Figure 2.2 shows the dispersion relation of SPP at a metal-dielectric flat interface. Here, the solid line represents the SPP dispersion curve, and the dashed one shows the dispersion curve of the propagating wave in the dielectric medium, known as the light line. Note that the dispersion curve of a SPP mode is located to the right of the dielectric light line, showing the momentum mismatching. This is the problem that a SPP cannot be excited by the direct illumination of light from the dielectric side. Besides, as ω approaches ω_{SPP}, the group velocity of SPP mode goes to zero. Since the decay rate is very high in either dielectric or metal region, a SPP form localized fluctuation at a metal-dielectric interface.

2.2 Localized surface plasmon (LSP)

The localized surface plasmon (LSP) occurs near the surface of some

metallic nanoparticles. The resonance of LSP depends mainly on the structure geometry and the polarization state of the incident light. Especially for nanoscale metallic geometry, such as a metallic sphere or a metallic circular cylinder, the LSP excitation is accompanied with a highly localized field around the nanostructure. Let us consider a metallic circular nano-cylinder in a homogeneous, linear, isotropic dielectric medium, under the illumination of visible light. Since the wavelength is much larger than the dimension of the circular cylinder, the quasi-static approximation is applicable to this problem. By solving Maxwell's equations and matching the associated boundary conditions, we can derive the formula for the LSP resonant frequency [24]

$$\omega_{LSP}^{circular\ cylinder} = \frac{\omega_p}{\sqrt{1 + \varepsilon_d}} .$$

(2.5)

For a single Ag circular cylinder embedded in GaN, the LSP resonant wavelength is at 430 nm. Note that the dielectric constant of GaN is set to be 6.25 in all the following simulations.

When the quasi-static approximation is not appropriate, the full Maxwell's equations have to be solved. For a sphere, the Mie theory has been well known [25]. For a circular cylinder, similar discussion can be found in [26].

Note that, in the microwave region, the metal can almost be regarded as a perfect electric conductor (PEC), and the phenomenon of SP is unclear. The SP mainly occurs in the visible spectral range for noble metals.

2.3 Dipole-SP coupling phenomenon

Okamoto et al. proposed possible mechanisms of quantum well (QW)-SP coupling and light extraction, as shown in Fig. 2.3 [1-3]. First, excitons are generated in the QW by photo-pumping or electrical-pumping. For a sample uncoated with metal, these excitons are terminated by the radiative (P_{rad}) or nonradiative (P_{non}) recombination rates, and the internal quantum efficiency (η_{int}) is defined as

$$\eta_{int} = P_{rad} / (P_{rad} + P_{non}) . \tag{2.6}$$

When a metallic layer is grown within the near-field of the active layer, and when the bandgap energy ($\hbar\omega_{BG}$) of InGaN active layer is close to the electron vibration energy ($\hbar\omega_{SP}$) of SP at the metal-semiconductor surface, then the QW energy can transfer to the SP. The photoluminescence (PL) decay rate is enhanced through the QW-SP coupling rate (P_{SP}), which is expected to be very fast. High electromagnetic field is produced by the large density of states from the SP dispersion diagram, making P_{SP}

increase. The QW-SP coupling in LED devices may be considered beneficial to the light extraction efficiency, because the SP can re-couple to radiate light by some specified fabrication. If the metallic surface is perfectly flat, the SP energy would be thermally dissipated without radiation. However, the SP energy can be extracted as light by providing roughness or nano-structuring the metallic layer. Such roughness provides SP additional momentum to scatter, to lose momentum, and to couple to radiation. The few tens of nanometer sized roughness in the Ag surface layer can be obtained by controlling the evaporation conditions or by microfabrication to obtain the high photon extraction efficiency.

In order to understand the strength of QW-SP coupling, Fermi's golden rule has been applied to estimate the transition probability or the recombination rate, $\Gamma_p(\omega)$ as

$$\Gamma_p(\omega) = \frac{1}{\tau} = \frac{2\pi}{\hbar} \left| \left\langle f \left| \vec{d} \cdot \vec{E}(\vec{r_e}) \right| i \right\rangle \right|^2 \rho(\hbar\omega) . \tag{2.7}$$

Here, τ is the spontaneous decay constant, $\left\langle f \left| \vec{d} \cdot \vec{E}(\vec{r_e}) \right| i \right\rangle$ is the dipole interaction matrix element and $\rho(\hbar\omega)$ is the plasmon mode density of states (DOS) [27, 28]. The density of states $\rho(\hbar\omega)$ can be obtained from the derivative $\frac{d(k^2)}{d\omega}$ of the dispersion relation $\omega(k)$ for a SP mode. Then Eq. (2.7) becomes

$$\Gamma_p(\omega) = \frac{2\pi}{\hbar} \left| \left\langle f \left| \vec{d} \cdot \vec{E}(\vec{r_e}) \right| i \right\rangle \right|^2 \left[\frac{L^2}{4\pi} \frac{d(k^2)}{d(\hbar\omega)} \right].$$

(2.8)

By increasing the density of states of a SP mode, the spontaneous recombination rate can be enhanced as the photon frequency of the active layer approaches the SP resonance frequency. Besides, when the active layer is closer to the metal-dielectric surface, the QW-SP coupling becomes stronger.
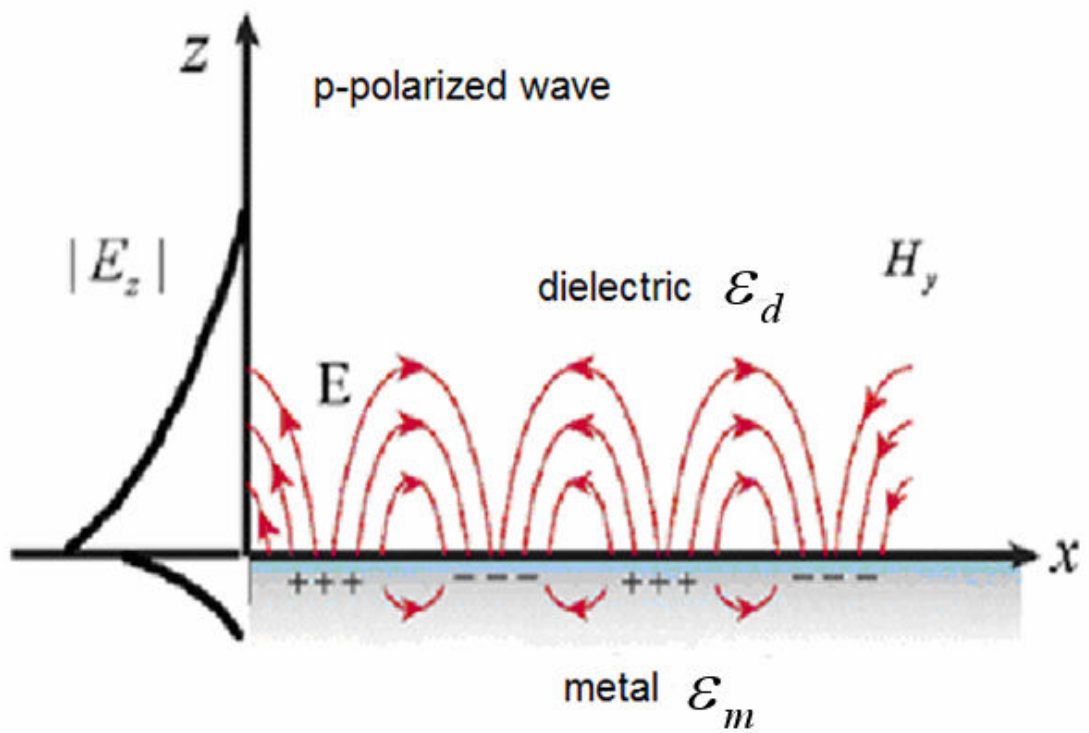
Fig. 2.1 Electric field distributions of a SPP at a metal-dielectric flat interface.
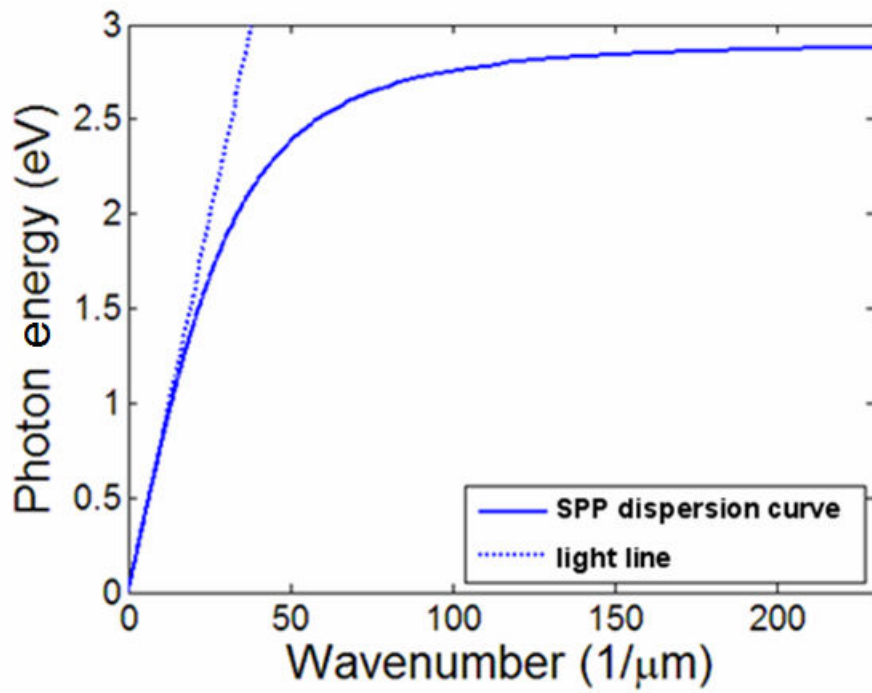
Fig. 2.2 SPP dispersion relation at a metal-dielectric flat interface.
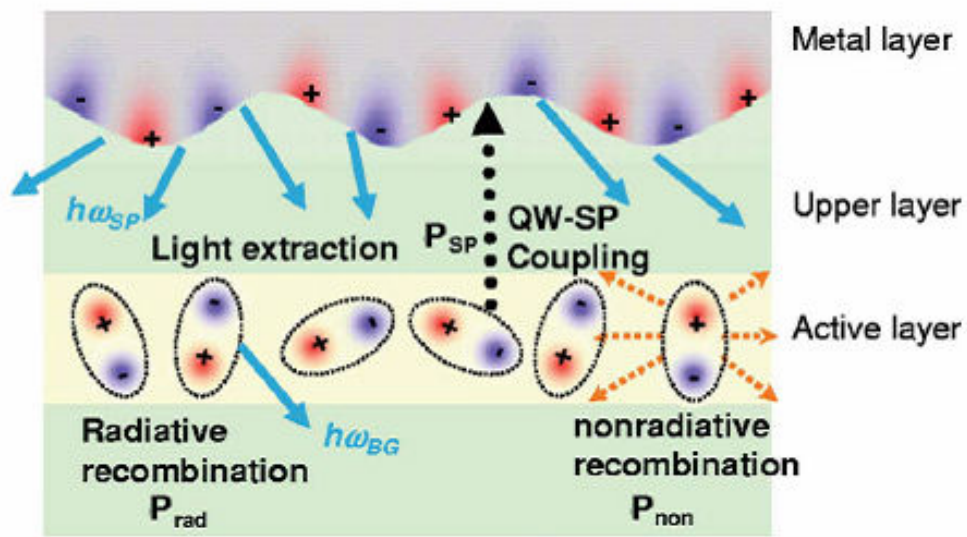
Fig. 2.3 Schematic diagram of the electron-hole recombination and QW-SP coupling.

Chapter 3
Numerical Methods

3.1 Boundary integral-equation method (BIEM)

The boundary integral-equation method used here is a 2D version of the surface integral-equation method based on the Stratton-Chu formulas [29-35]. The Stratton-Chu formulas state that the total field at an observation point $\bar{\rho}$, in an enclosed homogeneous, (ε, μ), region can be calculated as the sum of incident field and scattered field. The scattered field is produced by the equivalent electric and magnetic surface currents, $(\bar{J}, \bar{M})$, on all boundaries of this region. The expressions of the total fields are given by

$$
\begin{cases}
\bar{E}(\bar{\rho}) = \bar{E}_{inc}(\bar{\rho}) \\
\quad + \int \left\{ i\omega\mu\bar{J}(\bar{\rho}')\varphi(\bar{\rho},\bar{\rho}') - \bar{M}(\bar{\rho}')\times\nabla'\varphi(\bar{\rho},\bar{\rho}') - \left[\dfrac{i}{\omega\varepsilon}\nabla'\cdot\bar{J}(\bar{\rho}')\right]\nabla'\varphi(\bar{\rho},\bar{\rho}') \right\} dl' \\
\\
\bar{H}(\bar{\rho}) = \bar{H}_{inc}(\bar{\rho}) \\
\quad + \int \left\{ i\omega\varepsilon\bar{M}(\bar{\rho}')\varphi(\bar{\rho},\bar{\rho}') + \bar{J}(\bar{\rho}')\times\nabla'\varphi(\bar{\rho},\bar{\rho}') - \left[\dfrac{i}{\omega\mu}\nabla'\cdot\bar{M}(\bar{\rho}')\right]\nabla'\varphi(\bar{\rho},\bar{\rho}') \right\} dl'
\end{cases}
$$

.

$$(3.1)$$

Here, $\varphi(\bar{\rho},\bar{\rho}')$ is the 2D Green's function of the homogeneous region given by

$$\varphi(\bar{\rho}, \bar{\rho}') = \frac{i}{4} H_0^{(1)}(k|\bar{\rho} - \bar{\rho}'|), \tag{3.2}$$

where $H_0^{(1)}$ is the first-kind Hankel function of order zero, ω is the angular frequency, and $k = \omega\sqrt{\mu\varepsilon}$. Note that the time-harmonic variation of form $e^{-i\omega t}$ is assumed in this thesis.

If the observation point is located on a boundary (approaching from the interior of the region), then the electric and magnetic fields become

$$\begin{cases} \bar{E}(\bar{\rho}) = 2\bar{E}_{inc}(\bar{\rho}) \\ \quad + 2\int \left\{ i\omega\mu\bar{J}(\bar{\rho}')\varphi(\bar{\rho}, \bar{\rho}') - \bar{M}(\bar{\rho}') \times \nabla'\varphi(\bar{\rho}, \bar{\rho}') - \left[\frac{i}{\omega\varepsilon}\nabla' \cdot \bar{J}(\bar{\rho}')\right]\nabla'\varphi(\bar{\rho}, \bar{\rho}') \right\} dl' \\ \bar{H}(\bar{\rho}) = 2\bar{H}_{inc}(\bar{\rho}) \\ \quad + 2\int \left\{ i\omega\varepsilon\bar{M}(\bar{\rho}')\varphi(\bar{\rho}, \bar{\rho}') + \bar{J}(\bar{\rho}') \times \nabla'\varphi(\bar{\rho}, \bar{\rho}') - \left[\frac{i}{\omega\mu}\nabla' \cdot \bar{M}(\bar{\rho}')\right]\nabla'\varphi(\bar{\rho}, \bar{\rho}') \right\} dl' \end{cases}$$

$$\tag{3.3}$$

Note that the above line integrals are evaluated as the Cauchy principal values. Once the field expressions on each side of an interface approaching from different regions expressed by Eq. (3.3) are derived, we can match their tangential components to obtain a set of boundary integral equations associated with that interface.

Figure 3.1 shows a schematic diagram of a typical problem with a simple geometry containing only two regions. Region 2 is an infinitely extended background containing current sources $(\bar{J}_{inc}, \bar{M}_{inc})$ which

produce the incident fields, while region 1 is a scatterer without any source inside it. The boundary integral equations on interface C between the two regions can be derived as [35]

$$
\begin{cases}
\hat{n} \times \vec{E}_{inc} \\
\quad = \hat{n} \times \int_s \left[-i\omega \vec{J} \left(\mu_2 \phi_2 + \mu_1 \phi_1 \right) + \vec{M} \times \nabla'(\phi_2 + \phi_1) + \frac{i}{\omega} (\nabla' \cdot \vec{J}) \nabla' \left(\frac{\phi_2}{\varepsilon_2} + \frac{\phi_1}{\varepsilon_1} \right) \right] dl' \\
\hat{n} \times \vec{H}_{inc} \\
\quad = \hat{n} \times \int_s \left[-i\omega \vec{M} \left(\varepsilon_2 \phi_2 + \varepsilon_1 \phi_1 \right) - \vec{J} \times \nabla'(\phi_2 + \phi_1) + \frac{i}{\omega} \left[\nabla' \cdot \vec{M} \right] \nabla' \left(\frac{\phi_2}{\mu_2} + \frac{\phi_1}{\mu_1} \right) \right] dl'
\end{cases},
$$

$$(3.4)$$

where we define $\hat{n}$ as the unit normal vector of the boundary C pointing to R_2. Note that Eq. (3.4) is obtained by matching the tangential electric and magnetic fields on the two sides of C, with the fields expressed by Eq. (3.3).

To numerically solve the integral equation, one has to discretize the original problem into a matrix form. A commonly used technique is the method of moments (MoM), which expands the unknown equivalent surface currents $\left(\vec{J}, \vec{M} \right)$ with a set of local bases. The basis-expanded integral equation is further tested with the local bases (by Galerkin testing) and then transformed into a matrix equation.

In our formulation, the linear basis is used rather than the pulse basis, which often suffers from slow convergence, even for the all-dielectric

problems. Figure 3.2 (a) shows a boundary, on either side of which the equivalent surface currents, $\left(\bar{J}, \bar{M} \right)$ and $\left(-\bar{J}, -\bar{M} \right)$, are to be expanded with the linear bases. Here, a 2D transverse magnetic (TM) polarization, defined with field components E_x, E_y and H_z, is assumed. Figure 3.2 (b) is a discretized version of Fig. 3.2 (a). In Fig. 3.2 (b), the original smooth curve is approximated by several piecewise lines, with the nodes $\bar{\rho}_n$ used to define the linear basis. Two sets of linear bases $\bar{f}_j$ and $\bar{g}_j$ are used for expanding $\bar{J}$ and $\bar{M}$, respectively. Both $\bar{f}_j$ and $\bar{g}_j$ consist of two parts, i.e., $\bar{f}_j = \hat{t}_{j,1} f_{j,1} + \hat{t}_{j,2} f_{j,2}$ and $\bar{g}_j = \hat{z} \left(g_{j,1} + g_{j,2} \right)$, where $\hat{t}_{j,1}$ and $\hat{t}_{j,2}$ are unit tangent vectors defined by

$$\begin{cases} \hat{t}_{j,1} = \left(\bar{\rho}_j - \bar{\rho}_{j-1} \right) \big/ \left| \bar{\rho}_j - \bar{\rho}_{j-1} \right| \\ \\ \hat{t}_{j,2} = \left(\bar{\rho}_{j+1} - \bar{\rho}_j \right) \big/ \left| \bar{\rho}_{j+1} - \bar{\rho}_j \right| \end{cases} \tag{3.5}$$

so that $\hat{t}_{j,1(2)}$ is always pointed to the direction of ascending label number of the nodes. Also given below are the definitions of $f_{j,1}$ and $f_{j,2}$

$$f_{j,1} = \begin{cases} \dfrac{\left| \bar{\rho}' - \bar{\rho}_{j-1} \right|}{\left| \bar{\rho}_j - \bar{\rho}_{j-1} \right|}, & \bar{\rho}' \in \overline{\bar{\rho}_{j-1}\bar{\rho}_j} \\ 0, & \text{otherwise} \end{cases}, \qquad f_{j,2} = \begin{cases} \dfrac{\left| \bar{\rho}_{j+1} - \bar{\rho}' \right|}{\left| \bar{\rho}_{j+1} - \bar{\rho}_j \right|}, & \bar{\rho}' \in \overline{\bar{\rho}_j\bar{\rho}_{j+1}} \\ 0, & \text{otherwise} \end{cases}. \tag{3.6}$$

Note that $g_{j,1(2)} = f_{j,1(2)}$ is also defined.

Here a convention of the equivalent surface currents should be stated. We define the equivalent surface currents with positive sign in the following manner

$$\begin{cases} \bar{J} = \sum_j J_j \left(\hat{t}_{j,1} f_{j,1} + \hat{t}_{j,2} f_{j,2} \right) \\ \bar{M} = \hat{z} \sum_j M_j \left(g_{j,1} + g_{j,2} \right) \end{cases} .$$ (3.7)

Those with negative sign are denoted by $\left(-\bar{J}, \ -\bar{M} \right)$, with their definitions given below

$$\begin{cases} -\bar{J} = -\sum_j J_j \left(\hat{t}_{j,1} f_{j,1} + \hat{t}_{j,2} f_{j,2} \right) \\ -\bar{M} = -\hat{z} \sum_j M_j \left(g_{j,1} + g_{j,2} \right) \end{cases} .$$ (3.8)

Note that the directions of the equivalent surface currents plotted in Fig. 3.2 (a) do not really mean the true directions of the equivalent surface currents. The true directions of them are determined by the unknown coefficients, J_j and M_j, and the fixed unit vectors, $\hat{t}_{j,1}$, $\hat{t}_{j,2}$, and $\hat{z}$. Then the Galerkin testing procedure is used to execute the field expression on the interface, and we can transform the boundary integral equation into a matrix equation with the form of $[A]\vec{x} = \vec{b}$, Here the all elements of matrix $[A]$ are known after testing, column vector $\vec{b}$ represents the incident field, and column vector $\bar{x}$ represents unknown electric and magnetic currents. Once the equivalent surface currents are obtained through matrix inversion, the complex electromagnetic field at any position can be readily calculated through the boundary integral.

3.2 Simulated annealing method

How to find an optimal solution is an old problem, and it exists in various areas. Many mathematical techniques have been proposed to treat optimization problems [20, 21]. The simulated annealing (SA) method, which is related to the Monte Carlo method, is a useful algorithm for treating optimization problems. It not only has good efficiency for local searching but also is capable of searching a global extremum among several possible local extrema. The basic principles of the SA and how we apply it to synthesize metallic nanostructures will be described in the following.

3.2.1 Basic principles

The theory of SA algorithm stemmed from the pioneering work by Metropolis in 1953 [21]. In 1983, Kirkpatrick proposed this algorithm for solving the combinatorial optimization problem [20]. The SA is a probabilistic and iterative method of optimization mimicking the real annealing process of matter from the liquid state to the solid state. Initially, the temperature is high and the atoms of the liquid material are unstable in such high energy states. When the temperature is slowly decreased, the atoms will be gradually stabilized. If the temperature is

low enough, the material will become a perfect crystal in this low energy state. Similarly, an optimization problem can be posed as to find a state at which the cost function (analogous to the energy) attains a minimum.

To start with SA, we need to choose certain operation quantities, including an initial state and a cost function C. The latter changes its value at different states and is to be minimized. Also an appropriate temperature function T, whose value decreases with time, is selected. During the optimization process, the state is subject to a random change such that a new value of the cost function C is obtained. The probability, P, of choosing the new state to replace the old one is determined by ΔC, the difference between the new and old values of the cost function, as

$$P = \begin{cases} 1 & , & \text{if } \Delta C < 0 \\ e^{-\Delta C/T} & , & \text{if } \Delta C \geq 0 \end{cases} , \tag{3.9}$$

where the exponential form is adopted for initiating the Boltzmann distribution in thermodynamics. Based on Eq. (3.9), a better state of a lower cost value, i.e., $\Delta C < 0$, is accordingly preferred. When a worse state with the condition deviating away from the target occurs, i.e., $\Delta C \geq 0$, the selection is still implemented if $\exp(-\Delta C / T)$ is larger than a computer-generated random number between 0 and 1. In other words,

there is certain probability that we accept a worse state to avoid being trapped in a local minimum. Therefore, we reject the change of state if the cost function rises and the above judgment is not satisfied. After the evolution process mentioned above, the temperature T is decreased. We iterate such steps until the designated criterion is met. Figure 3.3 shows the flow chart of a general SA process.

Note that the efficiency of SA seriously depends on the initial state and the temperature profile. If the initial state is quite different from the optimal state, the iteration would be time-consuming. If the temperature decreases too rapidly, the worse result would hardly be accepted during the iteration and the state may be trapped in a local minimum. However, the slower the temperature decreases, the more iteration steps will be needed to achieve the optimization. Therefore, properly controlling the temperature and selecting the initial state would be crucial for obtaining a satisfactory optimization result efficiently.

3.2.2 Synthesis of metallic nanostructures by using simulated annealing method

Now, the SA is used to synthesize metallic nanostructures. In our simulation, the adjustable parameters include the radius r of each circular

cylinder (For each elliptical cylinder, we choose the length a of major semiaxis to adjust, and the length of minor semiaxis is fixed), the separation d between centers of the two circular or elliptical cylinders, the distance t from the center of each circular or elliptical cylinder to the plane of flat metal, and the vertical displacement h from the plane of flat metal to the dipole source. But in section 4.1, parameter h is fixed, unless specified otherwise. In every iteration, the probability of randomly adjusting these parameters by + 2 nm, - 2 nm, or 0 nm is equal. However, we randomly change parameter t by $0, \pm\frac{r}{10}$ with equal possibility in section 4.1. The cost function, in general, consists of two factors and the proportion of these two factors will be adjusted to keep their balanced weights in the cost function. Nevertheless, the cost function in section 4.1 is only as the negative value of downward emission.
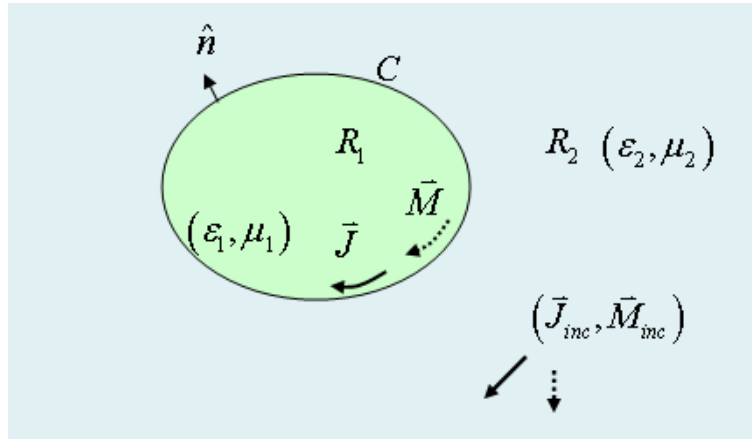
Fig. 3.1 Schematic diagram of a single-object scattering problem treated

by the BIEM.

(a)   (b)
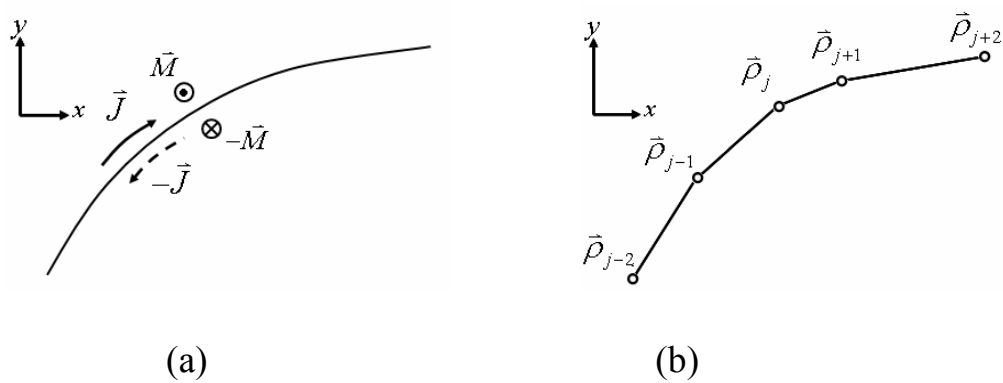
Fig. 3.2 (a) A boundary for applying the equivalent electric and magnetic

surface currents in a 2D TM case problem. (b) The discretized version of

(a).
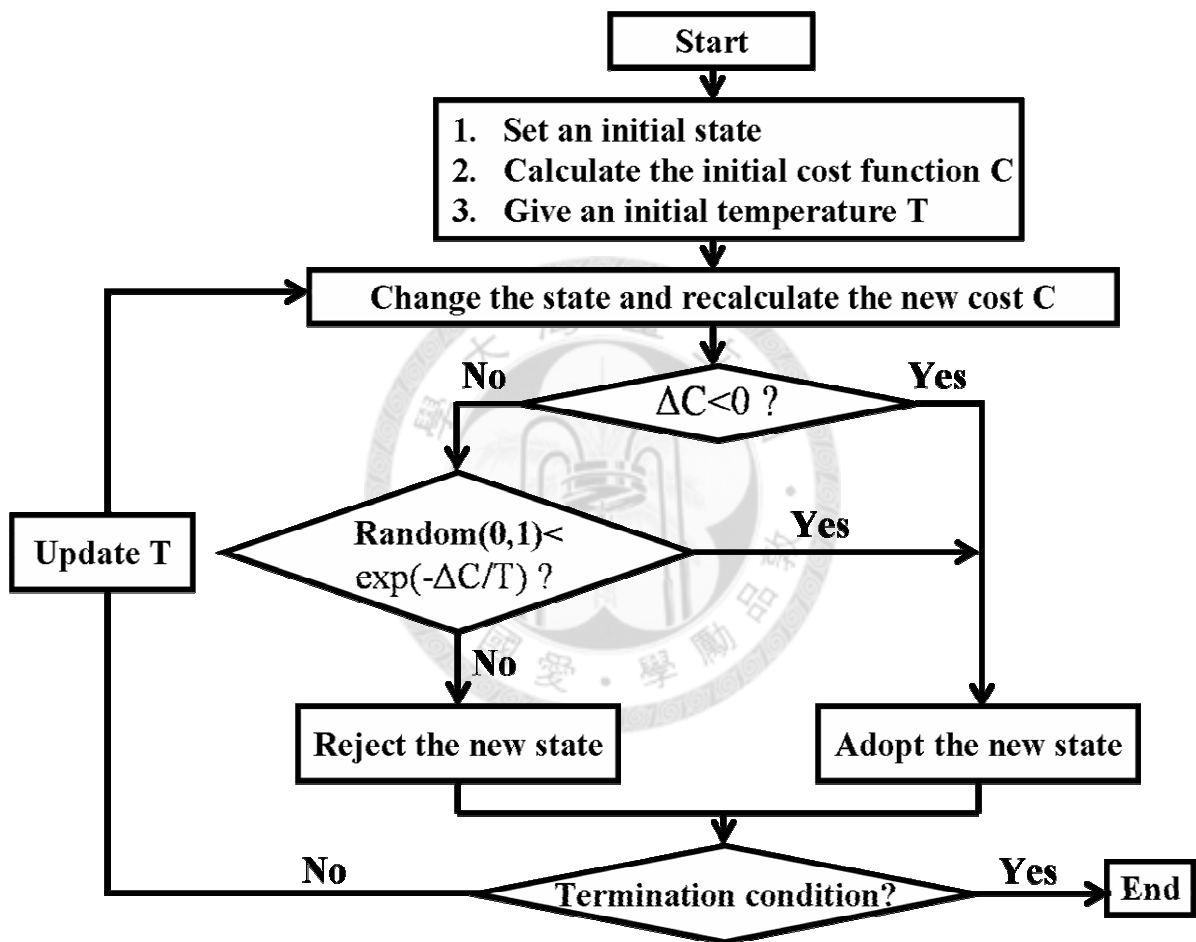
Fig. 3.3 Flow chart of a simulated annealing process.

Chapter 4
Numerical Results

4.1 Metallic nanostructures consisting of two circular cylinders partially embedded in a half-space

As mentioned in chapter 2, the SP modes can be classified as the SPP and LSP. It has been demonstrated that either SPP or LSP can individually enhance the dipole emission at its resonant wavelength [1-3]. However, the possibility of effective coupling between SPP and LSP at a common wavelength has not been discussed yet. Note that under the quasi-static approximation [23, 24], the LSP resonant wavelength of a single metallic circular cylinder is equal to the SPP resonant wavelength of a metallic half-space.

In this section, we synthesize a nanostructure consisting of two metallic circular cylinders partially embedded in a metallic half-space by the simulated annealing (SA) method. The nanostructure is so designed that the SPP and LSP couple effectively at their common resonant wavelength (435 nm), leading to the enhancement of the radiation of a nearby dipole source.

The parameter "downward emission" is defined as the power which

the dipole radiates in the direction away from the metallic structure in all the following simulations. We adjust the structure by the SA to maximize the downward emission at the resonant wavelength, with the cost function being the minus value of downward emission. Then the spectrum of downward emission for the optimal structure is calculated.

The insert of Fig. 4.1 shows the schematic structure which we try to optimize in this section. The structure and the x-directed dipole are infinitely extended along the z axis to form the two-dimensional problem in all the following simulations. Thus, the field components are E_x, E_y, and H_z only. The metal is Ag, and the surrounding dielectric is GaN in this section. Note that the dielectric in synthesized structures is set to be GaN in all the following simulations. All the adjustable parameters and the way of changing the structure are described in section 3.2.2. The plane of flat metal is set at y = 0 and the position of the dipole is set at (x, y) = (0, -h) in the following simulations. Note that we set h = r + t in this section, unless specified otherwise. We synthesize the optimal structures by adjusting these parameters to maximize the downward emission by using the SA method. After an iteration, if the downward emission of the new structure is larger than the old one, we accept the new structure.

Otherwise, we accept or reject the new structure according to the SA criterion described in chapter 3. It is well known that the SPP resonant frequency of a metallic half-space is $\frac{\omega_p}{\sqrt{1+\varepsilon_d}}$ [23], where ε_d is the dielectric constant of the surrounding dielectric. Based on the Drude model, we calculate the SPP resonant wavelength of the Ag-GaN flat interface to be at 430 nm. In our numerical simulation, however, a dipole cannot supply infinite wave numbers, so we choose a slightly longer wavelength at 435 nm for optimization. In order to manifest the advantage of the effective coupling between SPP and LSP, we also consider another structure for optimization at wavelength 520 nm for comparison. Through adjusting variable parameters, the optimal structure at wavelength 520 nm has mainly the LSP effect. We denote the structure optimized at 435 nm as structure A and that optimized at 520 nm as structure B. After optimization by the SA, the parameters of structure A are: r = 10 nm, d = 68 nm, t = 0.8 nm, h = 10.8 nm, and the parameters of structure B are: r = 14 nm, d = 60 nm, t = 7.6 nm, h = 21.6 nm.

Figure 4.1 shows the variation of downward emission during the iteration process. The green curve represents the chosen temperature distribution used in the SA process. The red curve shows the optimization

process for downward emission at wavelength 435 nm and the blue curve indicates the optimization process for downward emission at wavelength 520 nm. From these curves, we can find that these SA processes indeed converge to the optimal structures. Note that parameter r of structure B is larger than that of structure A. The reason is that as the resonant wavelength red shifts from 435 nm to 520 nm, the size of system should become bigger. There may be two ways for enlarging the size of system. One is to increase the separation between the two circular cylinders and the other is to increase the size of circular cylinders. Since the circular cylinders cannot be too far away from the source dipole for effectively exciting the LSP effect, the radius of circular cylinders then becomes larger for optimization at a longer wavelength.

Figure 4.2 shows the spectra of downward emission for structures A, B, and C. Here, the parameters of structure C are the same as those of structure A except that the dipole is moved downward by 10 nm, i.e., h = 20.8 nm. The y axis of solid curves is for the downward emission. The y axis of dashed curves is for the enhancement factor of downward emission. The enhancement factor is defined as the downward emission across the surface of y = -(60 + h) nm divided by the similar downward

emission when the structured Ag-GaN interface in the insert of Fig. 4.1 is replaced by a plane surface between Ag and GaN at y = 0. The black curves represent the spectra of structure A. The blue curves represent the spectra of structure B. The red curves represent the spectra of structure C. The peak value of downward emission for structure A occurs at wavelength 435 nm with peak value 0.025, and the peak enhancement factor is 6.12. The peak value of downward emission for structure B occurs at wavelength 520 nm with peak value 0.01, and the peak enhancement factor is 2.71. The peak value of downward emission for structure C occurs at wavelength 435 nm with peak value 0.009, and the peak enhancement factor is 2. The SA processes are successful because the peak of downward emission for each structure occurs indeed at the desired wavelength for optimization. We can find that both the peak value of downward emission and the peak enhancement factor of downward emission for structure A are bigger than those for structures B and C. This is consistent with the fact that at the resonant wavelength 435 nm, the SPP and LSP modes can couple effectively. Besides, structure B supports mainly the LSP mode because its resonant wavelength 520 nm is far away from the SPP resonant wavelength. The SPP and LSP modes for

structure C are both weak because the dipole is too far from the structure to effectively excite the SPP and LSP modes. Obviously, the peak value of downward emission and the peak enhancement factor of downward emission for structure C are less than those for structures A and B.

To further understand the coupling mechanism between SPP and LSP, we plot the distributions of the absolute values of magnetic field in Figs. 4.3 (a)-(d) for structure A at wavelength 435 nm (a), 404 nm (b), 465 nm (c), and 520 nm (d), and plot the distributions of the absolute values of electric field in Figs. 4.4 (a)-(d) for structure A at wavelength 435 nm (a), 404 nm (b), 465 nm (c), and 520 nm (d). The absolute value of electric field is calculated by the following formula in all the following simulations

$$\left|\vec{E}\right| = \sqrt{\left|E_x\right|^2 + \left|E_y\right|^2} \ . \tag{4.1}$$

The SP modes in Figs. 4.3 (a) and 4.4 (a) include both SPP and LSP, and the coupling effect between them is significant because at wavelength 435 nm both SPP and LSP resonate simultaneously. The field distributions are rather weak in Figs. 4.3 (b)-(d) and 4.4 (b)-(d), indicating that neither SPP nor LSP is effectively excited at these wavelengths for structure A.

Figure 4.5 shows the distributions of the absolute values of magnetic field (a) and electric field (b) at wavelength 520 nm for structure B. By comparing Fig. 4.5 (a) and Fig. 4.3 (d), we find that the LSP effect for structure B is more remarkable than that for structure A at wavelength 520 nm, leading to larger downward emission for structure B than that for structure A at wavelength 520 nm. However, as shown in Fig. 4.2, it is worth noting that the peak value of downward emission and the peak enhancement factor of downward emission for structure B at wavelength 520 nm are still smaller than those for structure A at wavelength 435 nm. The reason is that the SPP resonant wavelength for structure B is still at wavelength 435 nm but its LSP resonant wavelength now occurs at 520 nm. Therefore, the resonant coupling effect between SPP and LSP at a common wavelength is impossible. Shown in Figs. 4.6 (a) and (b) are the distributions of the absolute values of magnetic field (a) and electric field (b) for structure D at wavelength 435 nm. The parameters for structure D are: r = 20 nm, d = 68 nm, t = 0.8 nm, and h = 20.8 nm. Note that the radius of each circular cylinder is purposely enlarged to see its effect. The peak value of downward emission for structure D is only 0.0007. This reduction results from the fact that the SPP effect is weak due to the large

distance from dipole to flat metal and the LSP effect is also weak because the LSP resonant wavelength now is shifted away from 435 nm.

In summary, we have synthesized a metallic nanostructure (structure A), for which the SPP and LSP can couple effectively, to enhance the downward emission of a nearby dipole. The peak enhancement factor of downward emission for three structures A, B and C is listed Table 4.1, from which several conclusions can be drawn as follows. The emission enhancement is best when both SPP and LSP are excited and coupled at a common resonant wavelength. It becomes worse when only one of SPP or LSP is effectively excited and hence the coupling between SPP and LSP is weak. The emission enhancement is worst when both SPP and LSP are weak.

4.2 Metallic nanostructures consisting of a half-space and separate circular cylinders

For further investigating the SP effect, we try to synthesize the metallic nanostructures consisting of a Ag half-space and two separate circular cylinders, as the insert of Fig. 4.7. In this section, we try to synthesize a metallic nanostructure for application to white-light LEDs. Recently, most of the white-light LEDs in the market emit white light by

mixing blue light (wavelength 450 nm) and yellow light (wavelength 570 nm) [36]. Therefore, in this section the cost function is composed of downward emission at two wavelengths 450 nm and 570 nm.

In chapter 2 it is noted that the LSP resonant wavelength for a single thin Ag circular cylinder embedded in GaN is at 430 nm, near the desired blue light wavelength 450 nm. According to the assumed Drude model mentioned in chapter 2, the LSP resonant wavelength for a single thin Au circular cylinder embedded in GaN is at 540 nm, near the desired yellow light wavelength 570 nm. For the two separate circular cylinders considered here, the right one is Ag circular cylinder and the left is Au. To evoke the SA process, we denote the downward emission by ϕ in all the following simulations, and define the cost function C in this section as

$$C = -(\alpha \times \phi_{450} + (1-\alpha) \times \phi_{570}). \tag{4.2}$$

Here, ϕ_{450} represents the downward emission at wavelength 450 nm, and ϕ_{570} represents that at wavelength 570 nm. For balancing the relative proportion between ϕ_{450} and ϕ_{570} in the cost function, we adjust parameter α to let $\alpha \times \phi_{450}$ equal $(1-\alpha) \times \phi_{570}$ during the iteration process. After an iteration, if the cost function of the new structure is less than the old one, we accept the new structure. Otherwise, we accept or

reject the new structure according to the SA criterion described in chapter 3. Therefore, if the new structure is accepted, both ϕ_{450} and ϕ_{570} are changed and parameter α has to be adjusted again. All the adjustable parameters and the way of changing the structure are described in section 3.2.2. Note that the vertical position of the dipole source is kept separate from the bottom of the circular cylinders by at least 5 nm.

Figure 4.7 shows the variation of cost function in the iteration process. Here the solid curve represents the cost function and the dashed curve represents the chosen temperature distribution used in the SA process. Due to the sensitivity and importance of initial state for convergence, firstly, we do a SA process with an initial state and choose a better structure from those ever appearing in the iterations as a new initial state. Next, we re-start the SA process with the new initial state for reducing the number of iterations. Figure 4.7 is the result from the secondary SA process. In the figure, we can find that the SA process indeed converges to the optimal structure. The final optimal structure labeled as structure E is obtained through the SA with r = 10 nm, d = 32 nm, t = 24 nm, and h = 40 nm. Note that the vertical distance from dipole to the bottom of circular cylinders is 6 nm, slightly larger than 5 nm.

Figure 4.8 shows the variations of downward emission ϕ_{450} and ϕ_{570} at two wavelengths in the iteration process. Here the yellow solid curve represents the downward emission for yellow light, and the blue dashed curve represents that for blue light. In the figure, we can find that both ϕ_{450} and ϕ_{570} increase in the iteration process and reach the steady states.

Figure 4.9 shows the spectra of total emission and downward emission for structure E. The total emission is defined as the total outgoing power through a square of 2.5 nm in dimension centered at the dipole position in all the following simulations. Here the blue dashed curve represents the total emission, and the green solid curve represents the downward emission. In Fig. 4.9, we can find that there are two peaks in the spectrum of downward emission. One is at wavelength 450 nm with ϕ_{450} = 0.0072, and the other is at wavelength 565 nm with ϕ_{565} = 0.0181. This result is very consistent with our goal for SA.

Figure 4.10 shows the spectra of enhancement factor of total emission and downward emission for structure E. The enhancement factor of downward emission in this section is defined as the downward emission across the surface of y = -(60 + h) nm divided by the similar downward emission when the whole structure in the insert of Fig. 4.7 is

replaced by a Ag half-space in y > 0 and a GaN half-space in y < 0. The enhancement factor of total emission in this section is defined as the total emission divided by the similar total emission when the whole structure in the insert of Fig. 4.7 is replaced by a Ag half-space in y > 0 and a GaN half-space in y < 0. Here blue dashed curve represents the enhancement factor of total emission, and the green solid curve represents that of downward emission. In Fig. 4.10, there are also two peaks in the spectrum of enhancement factor of downward emission. One is at wavelength 450 nm with the enhancement factor 2.1, and the other is at wavelength 565 nm with the enhancement factor 5.1.

From the above simulation, we can find that structure E indeed has the potential for application to the white-light LEDs because of the enhancement of emission at wavelengths of both blue light and yellow light. To further investigate the mechanism of increasing emission for structure E at wavelengths of blue light and yellow light, we plot the distributions of the absolute values of magnetic field in Figs. 4.11 (a)-(d) at wavelength 435 nm (a), 450 nm (b), 540 nm (c), and 570 nm (d), respectively. In Figs. 4.11 (a) and (b), we can clearly observe the LSP resonance on the right Ag circular cylinder. This accounts for the

enhancement of emission for blue light (wavelength 450 nm). Similarly, another LSP resonance occurs on the left Au circular cylinder, as shown in Fig. 4.11 (c), contributing to the enhancement of emission for yellow light (wavelength 570 nm). Besides, we can find the LSP resonance of the system (mainly the two circular cylinders) occurs at wavelength 570 nm from the field distribution in Fig. 4.11 (d). This can help us understand why ϕ_{565} is larger than ϕ_{450}.

Figures 4.12 (a)-(d) are the distributions of the absolute values of electric field for structure E at wavelength 435 nm (a), 450 nm (b), 540 nm (c), and 570 nm (d), respectively. In Figs. 4.12 (a)-(d), we can see the resonance characteristics similar to Figs. 4.11 (a)-(d). For instance, we also observe the LSP resonance of the system at wavelength 570 nm in Fig. 4.12 (d).

For further investigating the roles of the two Ag and Au circular cylinders in the LSP resonant effect, we replace the left Au circular cylinder in structure E by a Ag circular cylinder and the original right Ag circular cylinder is unchanged. The new structure is called structure F.

Figure 4.13 shows the spectra of total emission and downward emission for structure F. Here the dashed curve represents total emission

and the solid one represents downward emission. The peaks of total emission and downward emission near wavelength 565 nm disappear. This confirms that the peaks near wavelength 565 nm for structure E is attributed to the LSP resonance on the left Au circular cylinder. Besides, the peak value of downward emission at wavelength 470 nm for structure F is larger than that at wavelength 450 nm for structure E. Note that the resonant wavelength red shifts from 430 nm (the LSP resonant wavelength for a single Ag circular cylinder embedded in GaN) to 470 nm because now the resonance is associated with the whole system consisting of two Ag circular cylinders and a Ag half-space.

Figure 4.14 shows the spectra of enhancement factor of total emission and downward emission for structure F. Obviously, the original peaks of enhancement factor of total emission and downward emission for structure E near wavelength 565 nm disappear for structure F. Figures 4.15 and 4.16 are respectively the distributions of the absolute values of magnetic field and electric field for structure F at wavelength 435 nm (a), 450 nm (b), 470 nm (c), 540 nm (d), and 570 nm (e). In these figures, we can clearly observe the resonant characteristic of strong local field near wavelength 450 nm. This corresponds to the LSP resonant wavelength

430 nm for a single Ag circular cylinder embedded in GaN.

In other aspect, we replace the right Ag circular cylinder in structure E by a Au circular cylinder and the original left Au circular cylinder is unchanged. The new structure is called structure G. Figure 4.17 shows the spectra of total emission and downward emission for structure G, and Fig. 4.18 shows the corresponding enhancement factor. Here the dashed curve represents total emission and the solid one represents downward emission. The peak of downward emission for structure G occurs at wavelength 580 nm, which is close to 565 nm. Therefore, we can confirm that the left Au circular cylinder is the cause for the peak of downward emission at wavelength 565 nm for structure E. By the way, the very weak peaks of total emission and downward emission near wavelength 430 nm for structure G is due to the SPP on Ag-GaN flat interface. Because the dipole is far away from the interface, the SPP effect is weak. The distributions of the absolute values of magnetic field and electric field for structure G at wavelength 435 nm (a), 450 nm (b), 540 nm (c), and 570 nm (d) are shown respectively in Figs. 4.19 (a)-(d) and 4.20 (a)-(d). In the figures, we can clearly notice the phenomenon of LSP near wavelength 570 nm. This is consistent with the deduction that the peak of downward

emission at wavelength 565 nm for structure E is mainly due to the LSP of left Au circular cylinder.

4.3 Metallic nanostructures consisting of a half-space and separate elliptical cylinders

In this section, we focus again on demonstrating the coupling behavior between SPP and LSP. The synthesized metallic nanostructure consists of two separate elliptical cylinders and a half-space, as shown in the insert of Fig. 4.21. All the adjustable parameters and the way of changing the structure are described in section 3.2.2. Note that the vertical position of the dipole source is kept to be separated from the bottom of the elliptical cylinders by at least 5 nm in all the following simulations. For effectively coupling between the SPP and LSP, the vertical position of the dipole source is kept not too far away from the half-space. Otherwise, the SPP cannot be excited. Therefore, we fix the length of minor semiaxis of elliptical cylinders to be 5 nm in all the following simulations. Besides, because the efficiency of the green-light LEDs in market is still low now, the cost function in this section is purposely composed of both the downward emission and the emission efficiency at a designated wavelength. The emission efficiency is defined

as the ratio of the downward emission to the total emission and we denote the emission efficiency by η in this section.

By adopting the Drude model for Au, we know that the SPP resonant wavelength for Au-GaN flat interface is at 540 nm. Therefore, the wavelength for optimization is set at 535 nm (near 540 nm). The cost function C is now defined as

$$C = -(\alpha \times \phi_{535} + (1-\alpha) \times \eta_{535}). \qquad (4.3)$$

Here, ϕ_{535} represents the downward emission at wavelength 535 nm, and η_{535} represents the emission efficiency at wavelength 535 nm. For balancing the relative proportion between ϕ_{535} and η_{535} in the cost function, we adjust parameter α to let $\alpha \times \phi_{535}$ equal $(1-\alpha) \times \eta_{535}$ during the iteration process. In this section, after an iteration, if the cost function of the new structure is less than the old one, we accept the new structure. Otherwise, we accept or reject the new structure according to the SA criterion described in chapter 3. In all the following simulations, the form of cost function and the way of adjusting parameter α are determined by Eq. (4.3). Note that the material of the half-space is Au and that of the two elliptical cylinders is Ag for the purpose of coupling SPP and LSP effectively at a common resonant wavelength 535 nm.

Figure 4.21 shows the variation of cost function in the iteration process. Here the solid curve represents the cost function and the dashed curve represents the chosen temperature distribution used in the SA process. In the figure, we can find that the SA process indeed converges to the optimal structure. The optimal structure is labeled as structure H. After optimization by the SA, the parameters of structure H are: a = 12 nm, d = 60 nm, t = 10 nm, h = 21 nm. Note that the vertical distance from dipole to the bottom of elliptical cylinders is 6 nm, slightly larger than 5 nm.

Figures 4.22 and 4.23 represent the variations of downward emission ϕ_{535} and emission efficiency η_{535}, respectively, in the iteration process. After the SA process, ϕ_{535} and η_{535} both converge to the values better than the initial values.

Figure 4.24 shows the spectra of total emission and downward emission for structure H. Here the dashed curve represents total emission and the solid one represents downward emission. In the figure, the peak of downward emission is at wavelength 525 nm. Its value is 0.014. Because the cost function is not dominated only by the downward emission, the peak of downward emission is not exactly at wavelength

535 nm.

Figure 4.25 represents the spectra of enhancement factor of total emission and downward emission for structure H. The enhancement factor of downward emission in this simulation is defined as the downward emission across the surface of y = -(60 + h) nm divided by the similar downward emission when the whole structure in the insert of Fig. 4.21 is replaced by a Au half-space in y > 0 and a GaN half-space in y < 0. The enhancement factor of total emission in this simulation is defined as the total emission divided by the similar total emission when the whole structure in the insert of Fig. 4.21 is replaced by a Au half-space in y > 0 and a GaN half-space in y < 0. The peak of enhancement factor of downward emission for structure H is at wavelength 530 nm. Its value is 3.753. Figure 4.26 represents the spectrum of emission efficiency for structure H. The maximum peak is at wavelength 400 nm because both the total emission and the downward emission at wavelength 400 nm are small. However, we can find another peak of emission efficiency at wavelength 535 nm. Its value is 0.7. This is consistent with the goal for SA. Through the high downward emission and emission efficiency for structure H near wavelength 535 nm, this can help the design of

green-light LEDs.

Note that in this case the downward emission and the emission efficiency can reach maxima almost simultaneously when the SPP and LSP couple effectively at a common resonant wavelength. This is our main objective in this section.

To further understand the coupling mechanism between SPP and LSP, we plot the distributions of the absolute values of magnetic field in Figs. 4.27 (a) and (b) for structure H at wavelength 435 nm (a) and 535 nm (b), and plot the distributions of the absolute values of electric field in Figs. 4.28 (a) and (b) at wavelength 435 nm (a) and 535 nm (b). In these figures, the characteristic of the SPP and LSP coupling at wavelength 535 nm is clearly seen. Besides, either the resonant wavelength for Ag-GaN flat interface (SPP) or that for a single Ag circular cylinder embedded in GaN (LSP) is at 430 nm. However, the structure H consists of two Ag elliptical cylinders embedded in GaN and a Au-GaN flat interface. Therefore, both the SPP and LSP are weak at wavelength 435 nm, as shown in Fig. 4.27 (a) and Fig. 4.28 (a).

In general, the SPP of metal-dielectric flat interface does not provide a direct mechanism to radiate into the dielectric region. However, the

total emission and downward emission at wavelength 525 nm for structure H is high. Next, we want to understand the role of SPP at the coupling process between SPP and LSP. For remaining the LSP effect, a new structure consisting of a Au half-space and two Ag elliptical cylinders, structure I, is simulated with the following parameters: t = 20 nm and h = 31 nm, and the others are the same with those of structure H. The distance from the dipole source to the half-space for structure I is larger than that for structure H, so the SPP effect is weaker. Figure 4.29 represents the spectra of total emission (dashed curve) and downward emission (solid curve) for structure I. The peak of downward emission red shifts to wavelength 555 nm due to the larger system than structure H. Its peak value is only 0.004. Note that the peak value of downward emission for structure H is 3.5 times larger than that for structure I. The reason is that the SPP can transfer energy to the LSP, and let the LSP have more radiation even though the SPP itself does not radiate. To confirm this viewpoint, we plot the distributions of the absolute values of magnetic field in Figs. 4.30 (a) and (b) for structure I at wavelength 535 nm (a) and 555 nm (b), and plot the distributions of the absolute values of electric field in Figs. 4.31 (a) and (b) at wavelength 535 nm (a) and 555

nm (b). In the figures, the phenomenon of energy transferring between SPP and LSP almost disappears because structure I does not provide an available path to couple the SPP and LSP effectively.

Next, we synthesize another structure consisting of two Ag elliptical cylinders and a Au half-space for optimization at wavelength 435 nm for comparison. The synthesized metallic nanostructure is shown in the insert of Fig. 4.32. Figure 4.32 shows the variation of cost function in the iteration process. Here the solid curve represents the cost function and the dashed curve represents the chosen temperature distribution used in the SA process. In the figure, we can find that the SA process indeed converges to the optimal structure. Through adjusting variable parameters, the optimal structure labeled as structure J mainly has the LSP effect at wavelength 435 nm. The parameters of structure J are: a = 6 nm, d = 24 nm, t = 20 nm, h = 39 nm. Note that the vertical distance from the dipole to the bottom of elliptical cylinders is 14 nm, larger than 5 nm.

Figures 4.33 and 4.34 represent the variations of downward emission ϕ_{435} and emission efficiency η_{435} in the iteration process. Being different from structure H, ϕ_{435} and η_{435}, after the SA process, do not simultaneously converge to the values better than the initial values for

structure J.

Figure 4.35 shows the spectra of total emission and downward emission for structure J. In the figure, we can find two peaks for downward emission at wavelengths 415 nm and 440 nm. The LSP resonant wavelength 430 nm of a single Ag circular cylinder embedded in GaN is now split into two because the two elliptical cylinders (nearly circular cylinders) couple significantly. Besides, the peak value of downward emission at wavelength 440 nm is smaller than that at wavelength 525 nm for structure H because structure J has only the LSP effect at wavelength 440 nm.

Figure 4.36 represents the spectra of enhancement factor of total emission and downward emission for structure J. The enhancement factor of downward emission in this simulation is defined as the downward emission across the surface of y = -(60 + h) nm divided by the similar downward emission when the whole structure in the insert of Fig. 4.32 is replaced by a Au half-space in y > 0 and a GaN half-space in y < 0. The enhancement factor of total emission in this simulation is defined as the total emission divided by the similar total emission when the whole structure in the insert of Fig. 4.32 is replaced by a Au half-space in y > 0

and a GaN half-space in y < 0. Note that the peak value of enhancement factor of downward emission for structure J is also smaller than that for structure H.

Figure 4.37 shows the spectrum of emission efficiency for structure J. In the figure, the peak of emission efficiency is at wavelength 465 nm, not at wavelength 435 nm. We find that the downward emission and the emission efficiency cannot reach maxima simultaneously when the SPP and LSP do not effectively couple at a common resonant wavelength. This will be confirmed and discussed in the later development. By the way, the value of emission efficiency at wavelength 435 nm for structure J is smaller than that at wavelength 535 nm for structure H. It is because that the LSP resonant wavelength for a single Ag circular cylinder embedded in GaN is also near 435 nm. This leads to the large metal dissipation for structure J near the resonant wavelength so that the emission efficiency decreases.

Figures 4.38 and 4.39 respectively show the distributions of the absolute values of magnetic field and electric field for structure J at wavelength 415 nm (a), 435 nm (b), and 440 nm (c). In the figures, we can find that the SPP effect is so weak that the SPP and LSP do not

couple effectively and the local field is large inside the Ag elliptical cylinders. These characteristics are consistent with our deductions in the context.

To reconfirm that the downward emission and the emission efficiency can reach maxima almost simultaneously when the SPP and LSP couple effectively at a common resonant wavelength, with unchanged two Ag elliptical cylinders, we replace the Au half-space by the Ag one to construct new structures for optimization in the following simulations, as the insert of Fig. 4.40. We firstly optimize a structure at wavelength 435 nm. Figure 4.40 shows the variation of cost function in the iteration process. Here the solid curve represents the cost function and the dashed curve represents the chosen temperature distribution used in the SA process. The final optimal structure labeled as structure K is obtained through the SA with parameters a = 6 nm, d = 24 nm, t = 12 nm, and h = 37 nm. Note that the vertical distance from the dipole to the bottom of elliptical cylinders is 20 nm, quite larger than 5 nm.

Figure 4.41 represents the spectra of total emission and downward emission for structure K. The peak of downward emission for structure K is at wavelength 440 nm (near 435 nm). Note that its value is only 0.007.

Figure 4.42 shows the spectra of enhancement factor of total emission and downward emission for structure K. The enhancement factor of downward emission in this simulation is defined as the downward emission across the surface of y = -(60 + h) nm divided by the similar downward emission when the whole structure in the insert of Fig. 4.40 is replaced by a Ag half-space in y > 0 and a GaN half-space in y < 0. The enhancement factor of total emission in this simulation is defined as the total emission divided by the similar total emission when the whole structure in the insert of Fig. 4.40 is replaced by a Ag half-space in y > 0 and a GaN half-space in y < 0. The peak value of enhancement factor of downward emission for structure K at wavelength 440 nm is 1.85.

Figure 4.43 shows the spectrum of emission efficiency for structure K. The maximum peak of emission efficiency for structure K occurs at wavelength 410 nm, and another peak is at wavelength 435 nm with its value 0.72. This confirms again that the downward emission and the emission efficiency can reach maxima almost simultaneously when the SPP and LSP effectively couple at a common resonant wavelength. Note that the LSP for structure K is not only the LSP of the whole system but also the LSP of a single Ag circular cylinder embedded in GaN. For

enhancing the emission efficiency, the metal dissipation should be small. This can be accomplished by increasing the vertical distance from the dipole source to the bottom of elliptical cylinders, but this also decreases the downward emission. Apparently, there is a trade-off between optimizing the downward emission and the emission efficiency for certain structures whose LSP of the whole system and LSP of a single metallic nanoparticle are resonant at a common designated wavelength.

Figures 4.44 (a) and (b) are respectively the distributions of the absolute values of magnetic field (a) and electric field (b) for structure K at wavelength 435 nm. In the figures, we can observe both the SPP and LSP relatively weak since the vertical distance from the dipole to the elliptical cylinders is far. Compared to Fig. 4.39, the local field inside two elliptical cylinders is smaller for structure K than that for structure J. This leads to higher emission efficiency at wavelength 435 nm for structure K as compared with structure J.

For further comparison, we next choose wavelength 535 nm for optimization. The synthesized metallic nanostructure whose material is the same with structure K is shown in the insert of Fig. 4.45. Figure 4.45 shows the variation of cost function in the iteration process. Here the

solid curve represents the cost function and the dashed curve represents the chosen temperature distribution used in the SA process. In the figure, we can find that the SA process indeed converges to the optimal structure. The final optimal structure labeled as structure L is obtained through the SA with parameters $a = 14$ nm, $d = 72$ nm, $t = 12$ nm, and $h = 27$ nm. Note the distance d between centers of the two elliptical cylinders and the length a of major semiaxis of each elliptical cylinder are both enlarged, corresponding to a large resonant wavelength.

Figure 4.46 represents the spectra of total emission and downward emission for structure L. Structure L has mainly the LSP effect near the designated wavelength 535 nm. The peak of downward emission is at wavelength 525 nm. Its value is much smaller than that for structure H since the SPP and LSP do not couple effectively at a common resonant wavelength for structure L.

Figure 4.47 shows the spectrum of emission efficiency for structure L. The peak of emission efficiency for structure L is at wavelength 400 nm. This again confirms that the downward emission and the emission efficiency cannot reach maxima simultaneously when the SPP and LSP do not effectively couple at a common resonant wavelength.

Figures 4.48 and 4.49 are respectively the distributions of the absolute values of magnetic field and electric field for structure L at wavelength 435 nm (a) and 535 nm (b). In Figs. 4.48 (b) and 4.49 (b) the LSP characteristic can be clearly observed and the SPP is weak.

To summarize, Table 4.2 lists parameters for all structures discussed in this section (except for next structure M). In the table, we can find that structure H is the best one. For structure H, both the SPP and LSP couple effectively at a common resonant wavelength. Note that the LSP is the one associated with the whole system. Therefore, the downward emission and the emission efficiency can reach maxima almost simultaneously at a common resonant wavelength 535 nm.

Finally, for practical purpose, we simulate a metallic nanostructure labeled as structure M, as shown in Fig. 4.50. It is composed of four Ag elliptical cylinders embedded in GaN and a Au half-space. The size of each elliptical cylinder is same as that for structure H. The separation between centers of adjacent elliptical cylinders is 60 nm, the distance from the center of each elliptical cylinder to the plane of flat metal is 10 nm, and the vertical displacement from the metallic half-space to the dipole source is 21 nm.

Figure 4.51 represents the variations of total emission and downward emission for structure M at wavelength 535 nm with the horizontal position of the dipole source. The average values of total emission and downward emission respectively are 0.013 and 0.006, respectively.

Figure 4.52 shows the variations of enhancement factor of total emission and downward emission for structure M at wavelength 535 nm with the horizontal position of the dipole source. The enhancement factor of downward emission in this simulation is defined as the downward emission across the surface of $y = -(60 + h)$ nm divided by the similar downward emission when the whole structure in the Fig. 4.50 is replaced by a Au half-space in $y > 0$ and a GaN half-space in $y < 0$. The enhancement factor of total emission in this simulation is defined as the total emission divided by the similar total emission when the whole structure in the Fig. 4.50 is replaced by a Au half-space in $y > 0$ and a GaN half-space in $y < 0$. The average values of enhancement factor of total emission and downward emission are 2.06 and 1.65, respectively. This demonstrates that these optimal structures we discussed are indeed useful for practical applications.

Table 4.1 Peak enhancement factors of downward emission for three

structures in a spectral range from 400 nm to 700 nm.

	d (nm)	r (nm)	t (nm)	h (nm)	peak enhancement factor of downward emission
Structure A	68	10	0.8	10.8	6.12
Structure B	60	14	7.6	21.6	2.71
Structure C	68	10	0.8	20.8	2

Table 4.2 Parameters for all structures discussed in section 4.3 (except for

structure M) and their downward emission peak values and the

corresponding wavelengths.

	metallic half-space	elliptical cylinders	a (nm)	d (nm)	t (nm)	h (nm)	downward emission peak value / wavelength
Structure H	Au	Ag	12	60	10	21	0.014 / 525 nm
Structure I	Au	Ag	12	60	20	31	0.004 / 555 nm
Structure J	Au	Ag	6	24	20	39	0.01 / 440 nm
Structure K	Ag	Ag	6	24	12	37	0.007 / 440 nm
Structure L	Ag	Ag	14	72	12	27	0.005 / 525 nm
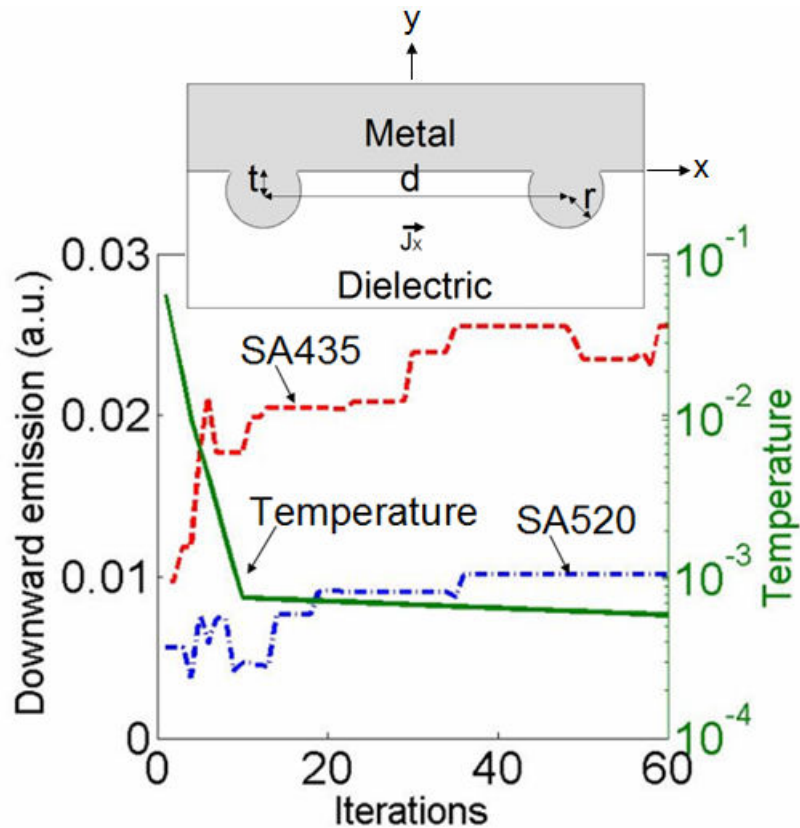
Fig. 4.1 Variation of downward emission during the iteration process. The green curve represents the chosen temperature distribution used in the SA process. The red curve shows the optimization process for downward emission at wavelength 435 nm and the blue curve indicates the optimization process for downward emission at wavelength 520 nm. The synthetic Ag-GaN interface geometry is shown schematically in the insert. An x-oriented dipole, denoted by an arrow and labeled by J_x, is located at $(x, y) = (0, -h)$. The flat part of Ag-GaN interface is at $y = 0$.
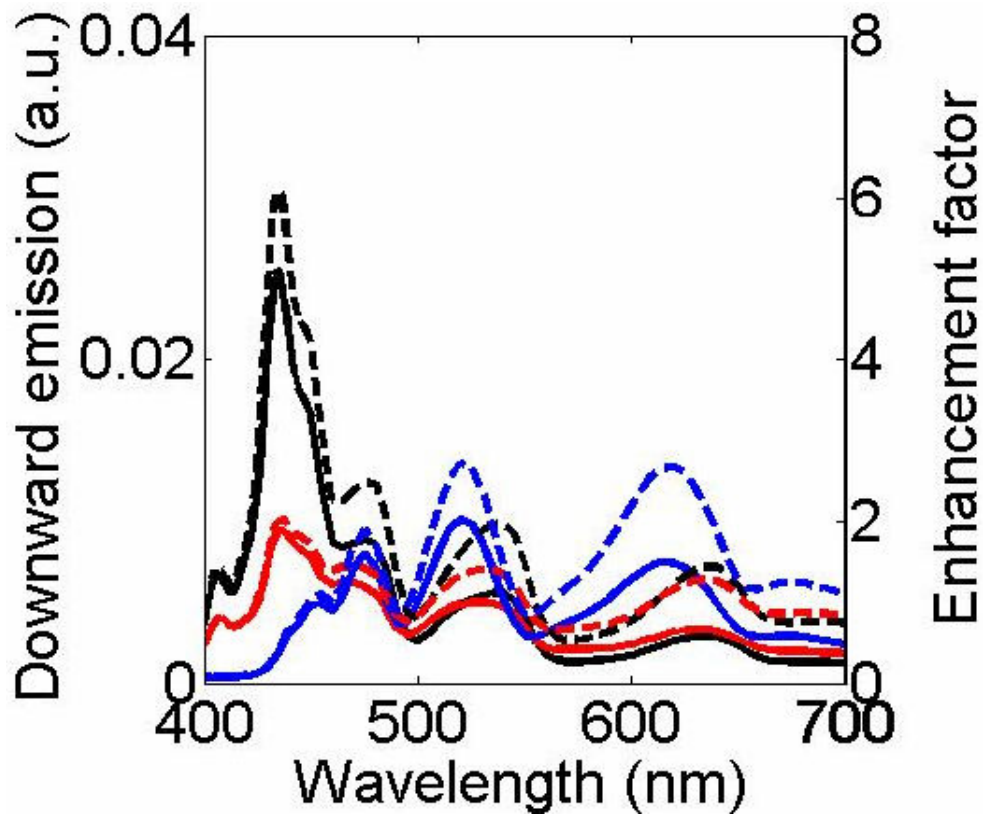
Fig. 4.2 Spectra of downward emission and enhancement factor of downward emission for three different structures. The black curves represent the spectra of structure A. The blue curves represent the spectra of structure B. The red curves represent the spectra of structure C. The y axis of solid curves is for the downward emission. The y axis of dashed curves is for the enhancement factor of downward emission.
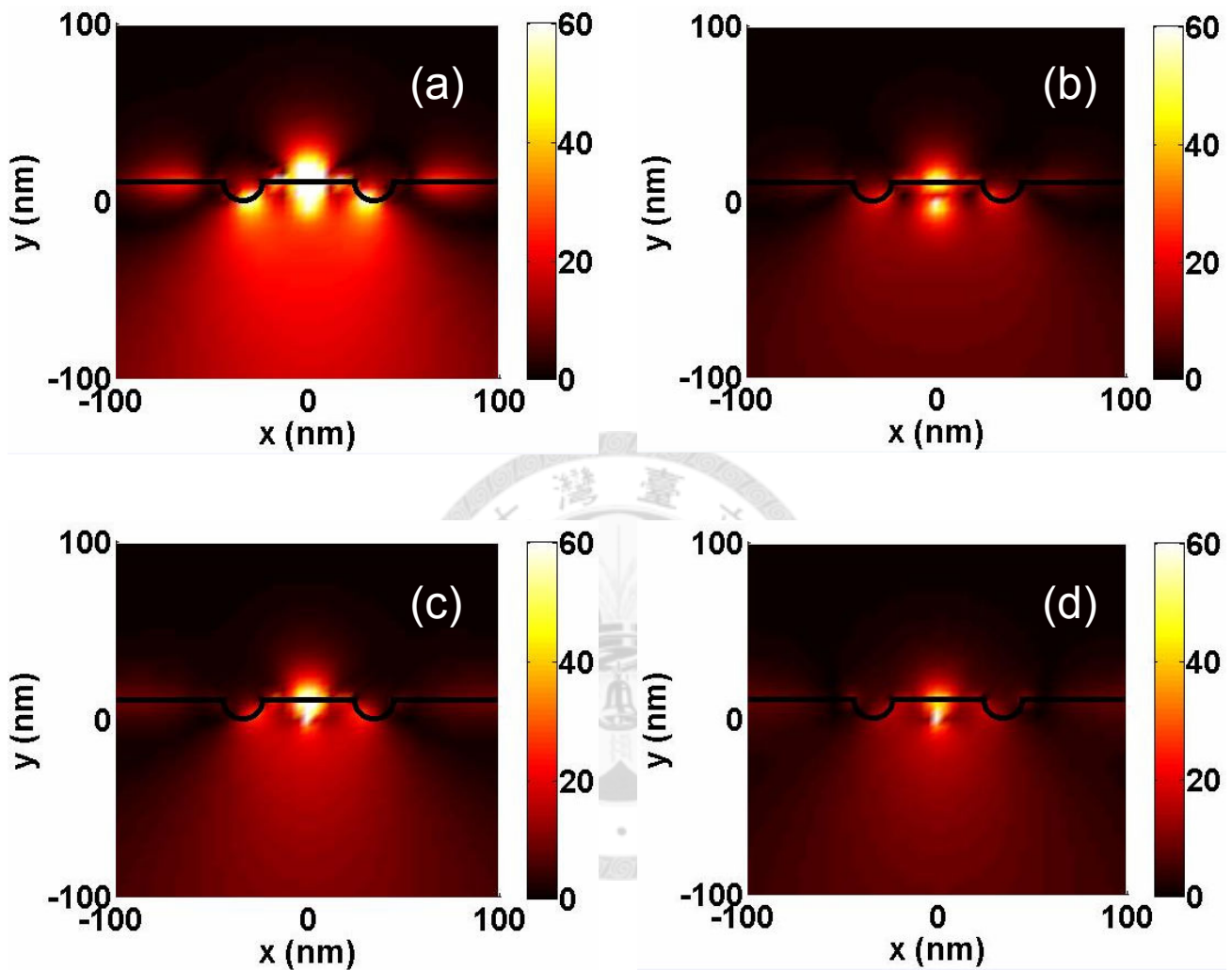
Fig. 4.3 Distributions of the absolute values of magnetic field for structure A at wavelength 435 nm (a), 404 nm (b), 465 nm (c), and 520 nm (d).
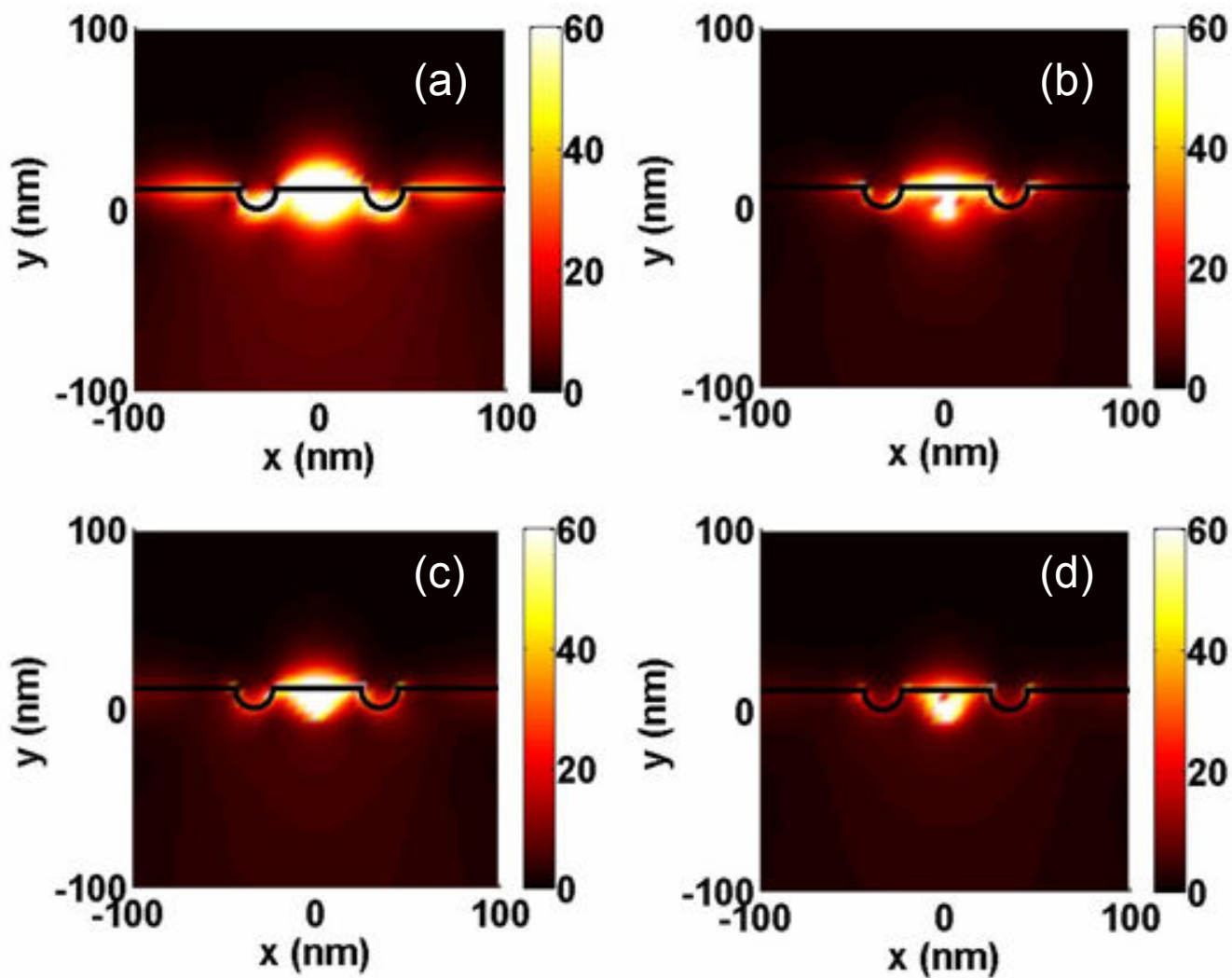
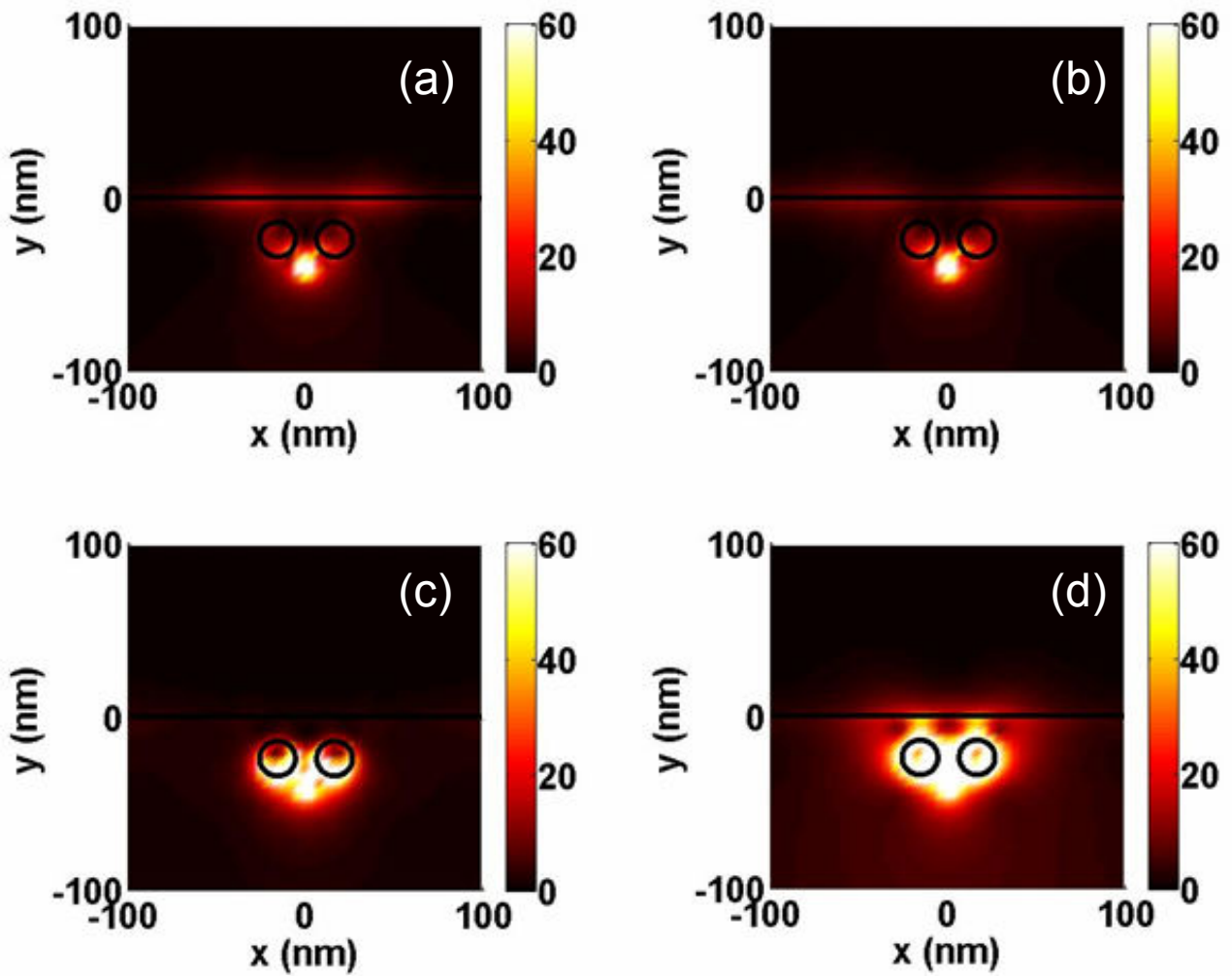Fig. 4.4 Distributions of the absolute values of electric field for structure

A at wavelength 435 nm (a), 404 nm (b), 465 nm (c), and 520 nm (d).
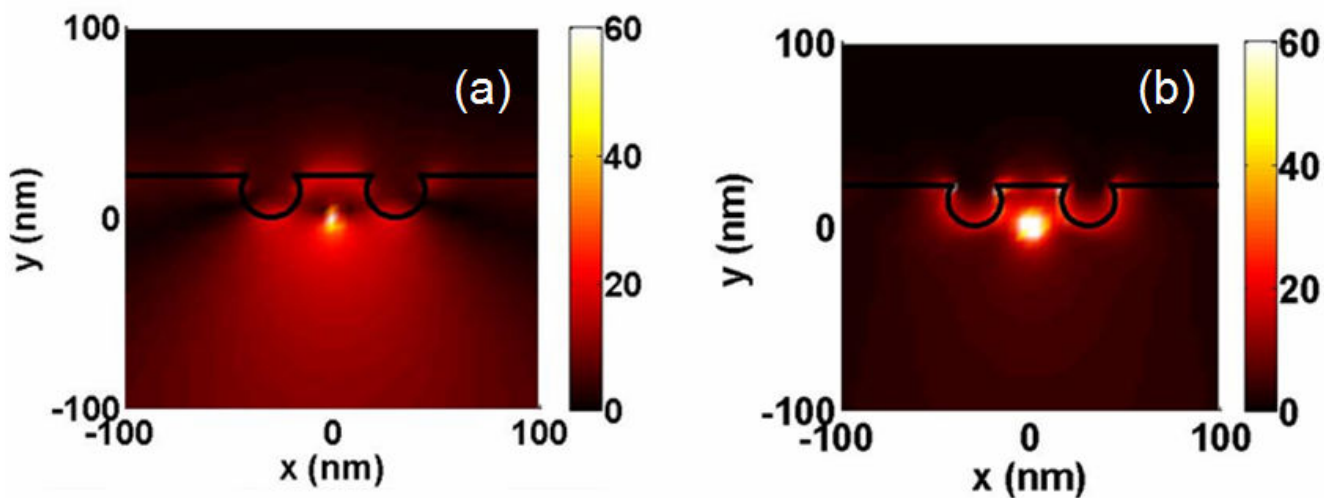
Fig. 4.5 Distributions of the absolute values of magnetic field (a) and electric field (b) for structure B at wavelength 520 nm.
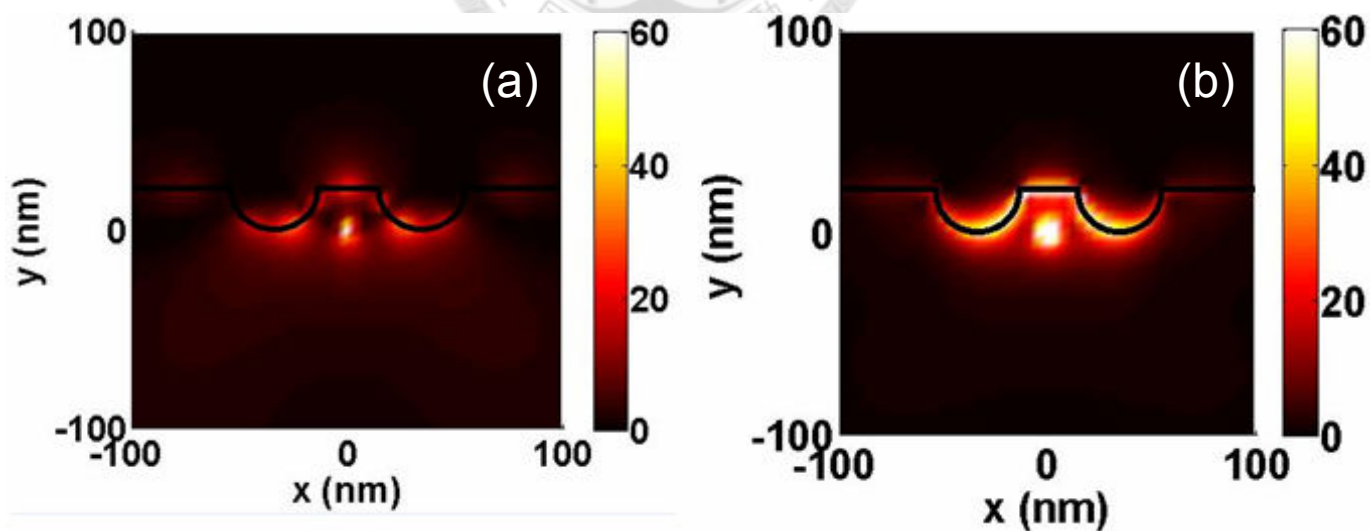
Fig. 4.6 Distributions of the absolute values of magnetic field (a) and electric field (b) for structure D at wavelength 435 nm.
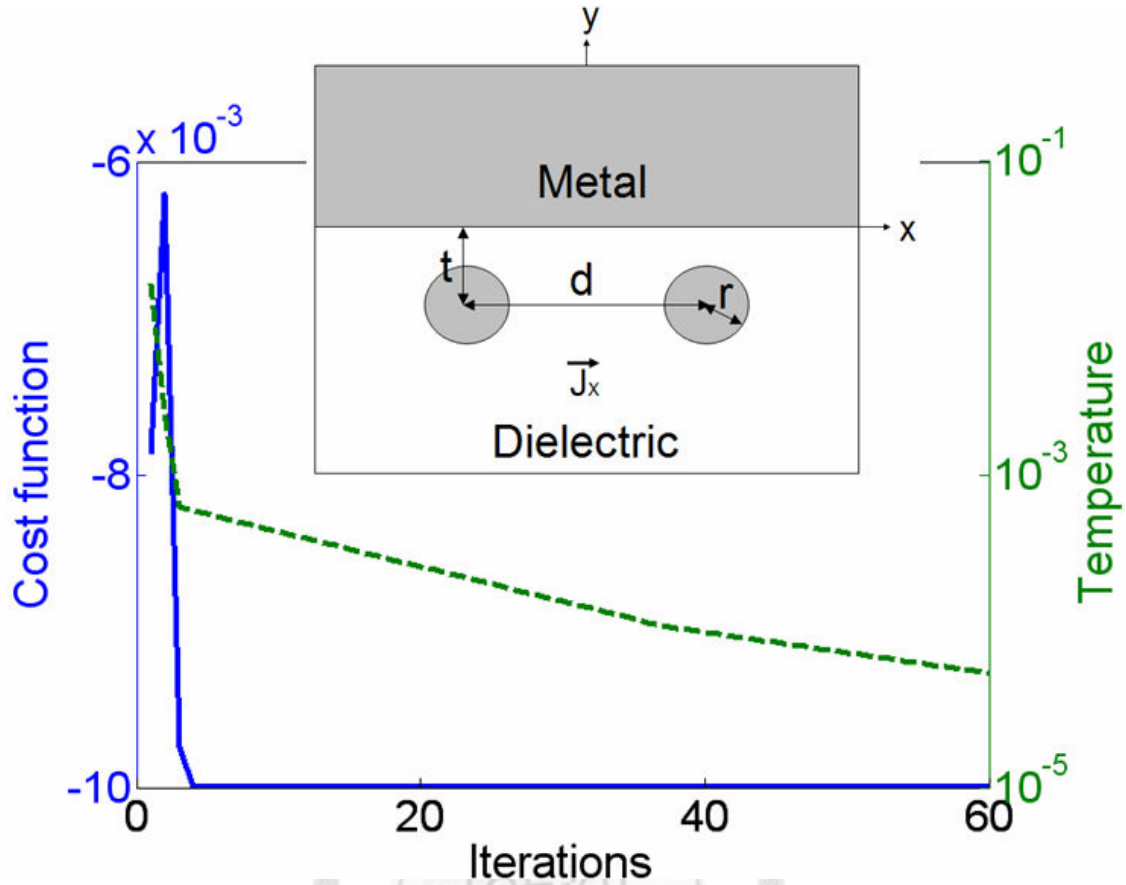
Fig. 4.7 Variation of cost function in the iteration process. The solid curve represents the cost function and the dashed curve represents the chosen temperature distribution used in the SA process. The synthetic structure is shown schematically in the insert. An x-oriented dipole, denoted by an arrow and labeled by J_x, is located at $(x, y) = (0, -h)$. The metal-dielectric flat interface is at $y = 0$.
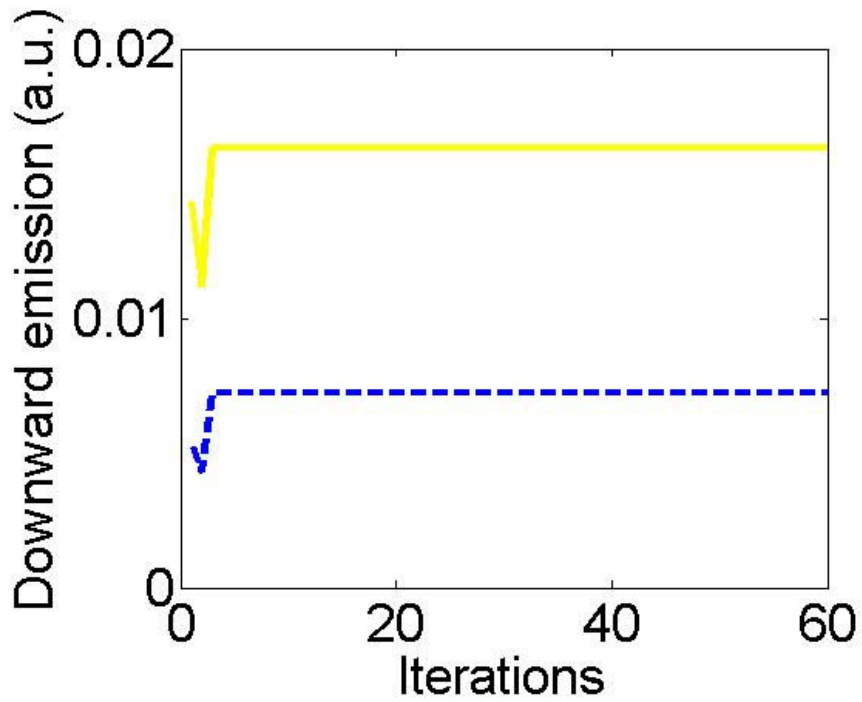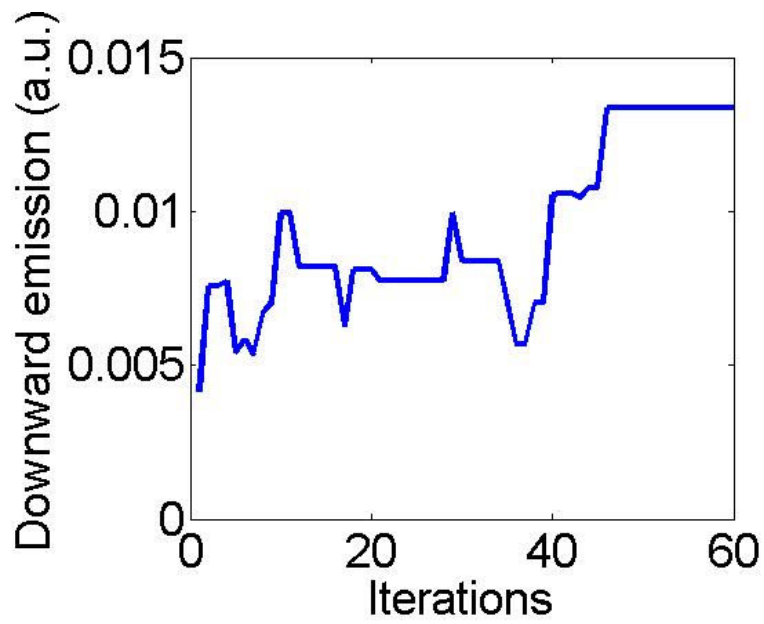
Fig. 4.8 Variations of downward emission at two wavelengths 450 nm and 570 nm in the iteration process. The dashed curve represents the downward emission at wavelength 450 nm, and the solid curve represents that at wavelength 570 nm.
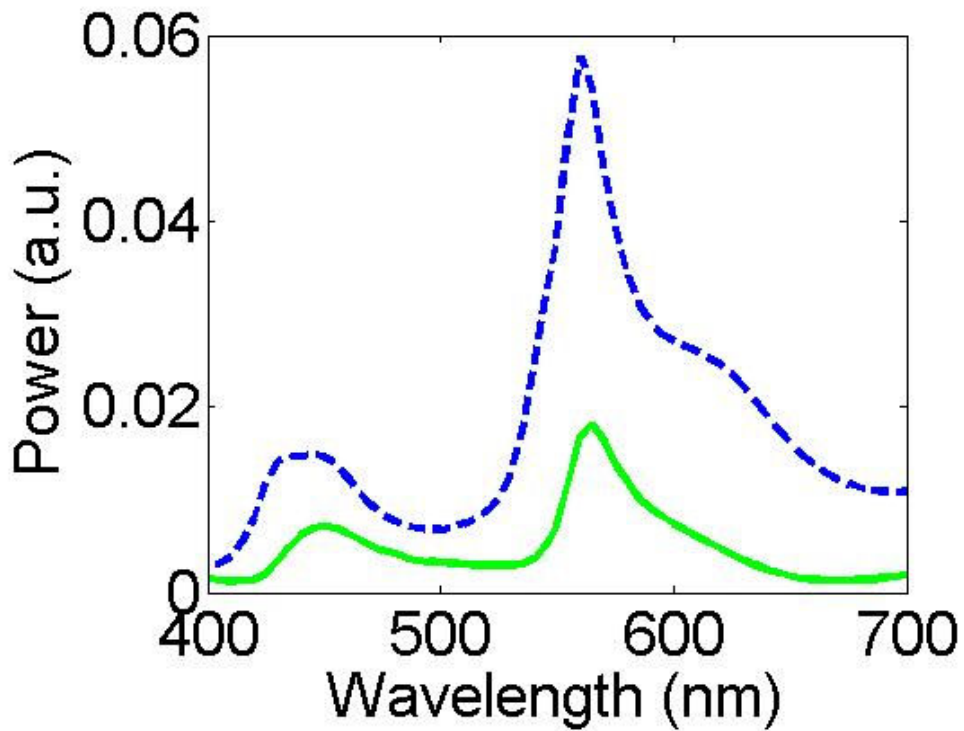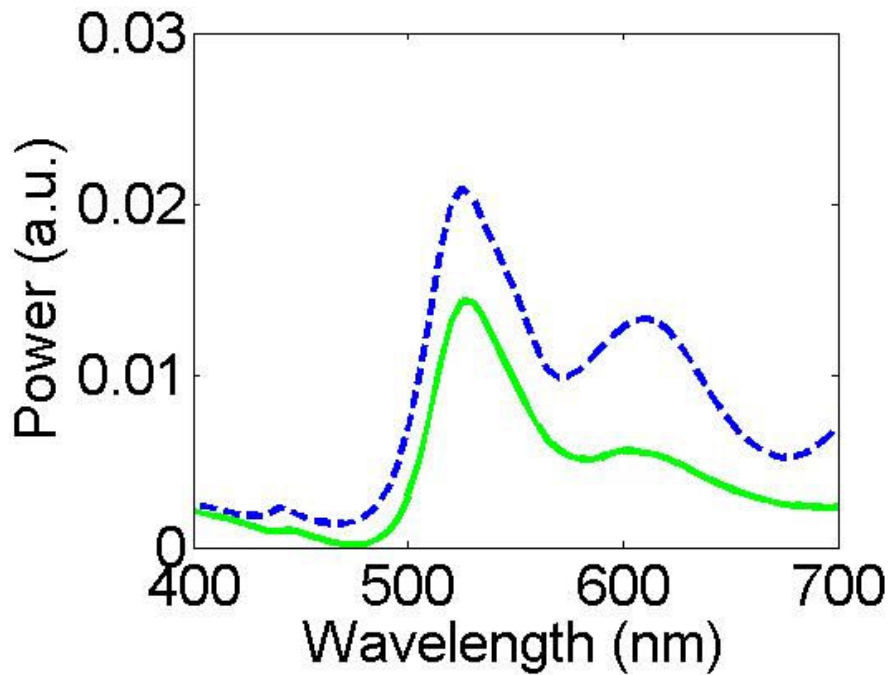
Fig. 4.9 Spectra of total emission (dashed curve) and downward emission
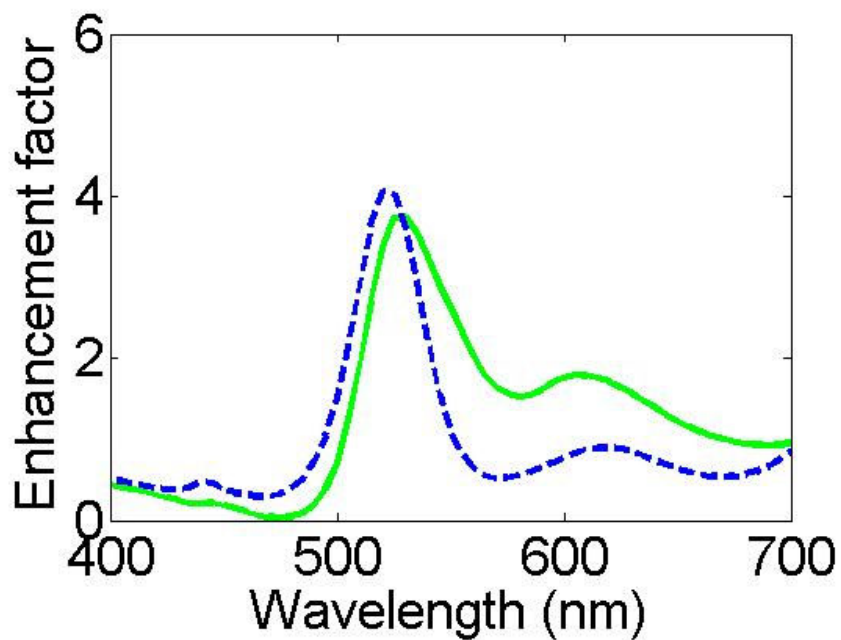
(solid curve) for structure E.
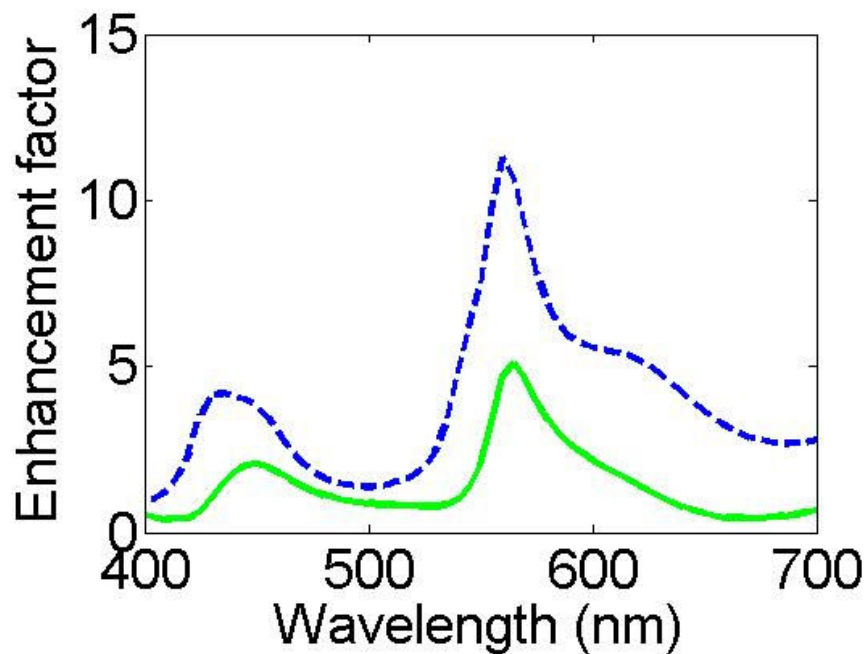
Fig. 4.10 Spectra of enhancement factor of total emission (dashed curve)

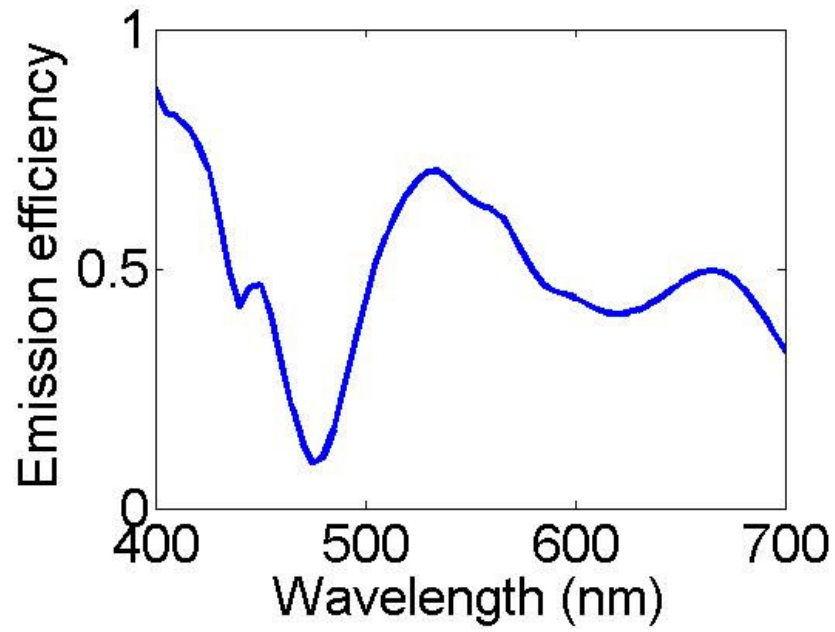and downward emission (solid curve) for structure E.
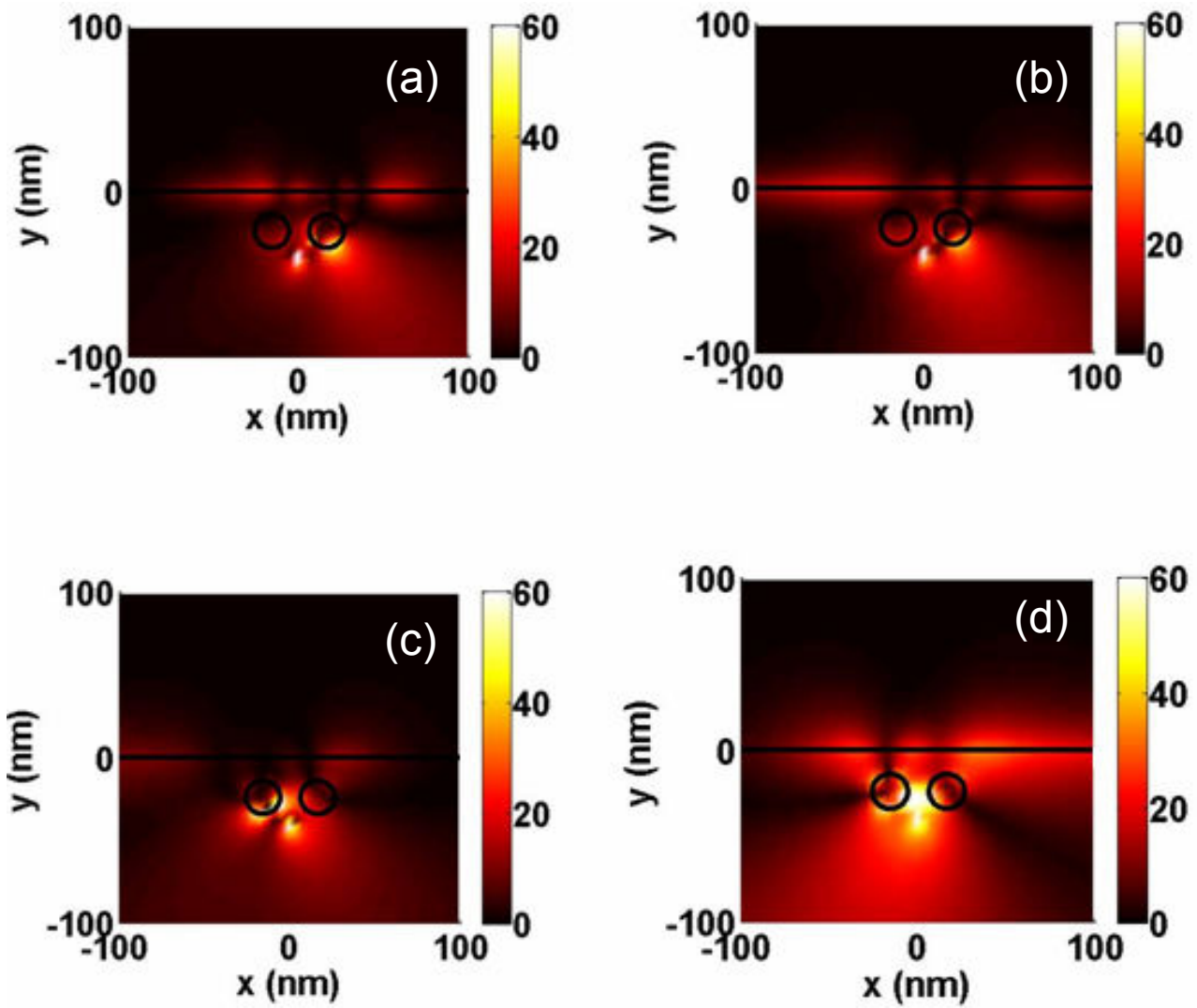
Fig. 4.11 Distributions of the absolute values of magnetic field for structure E at wavelength 435 nm (a), 450 nm (b), 540 nm (c), and 570 nm (d).
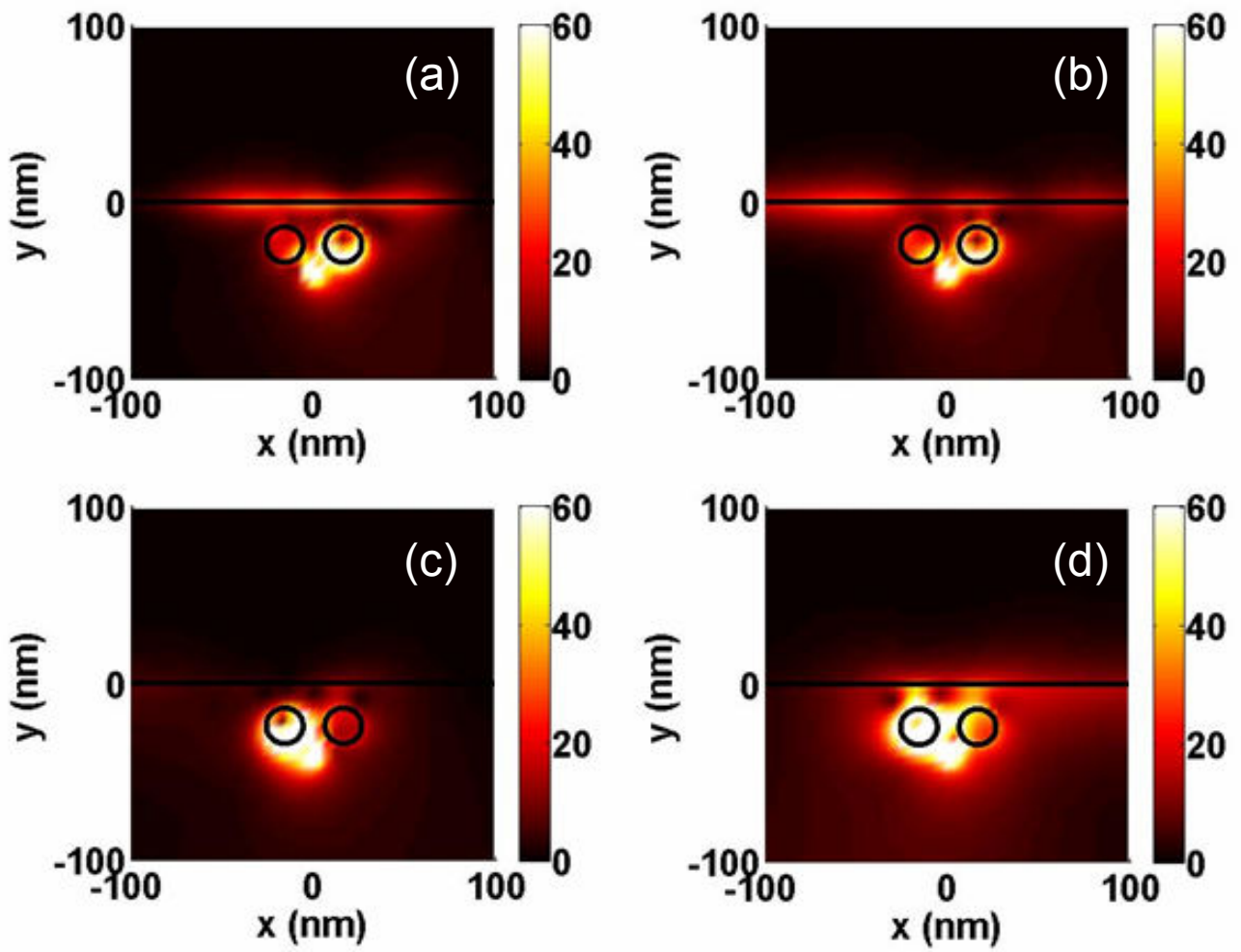
Fig. 4.12 Distributions of the absolute values of electric field for structure

E at wavelength 435 nm (a), 450 nm (b), 540 nm (c), and 570 nm (d).
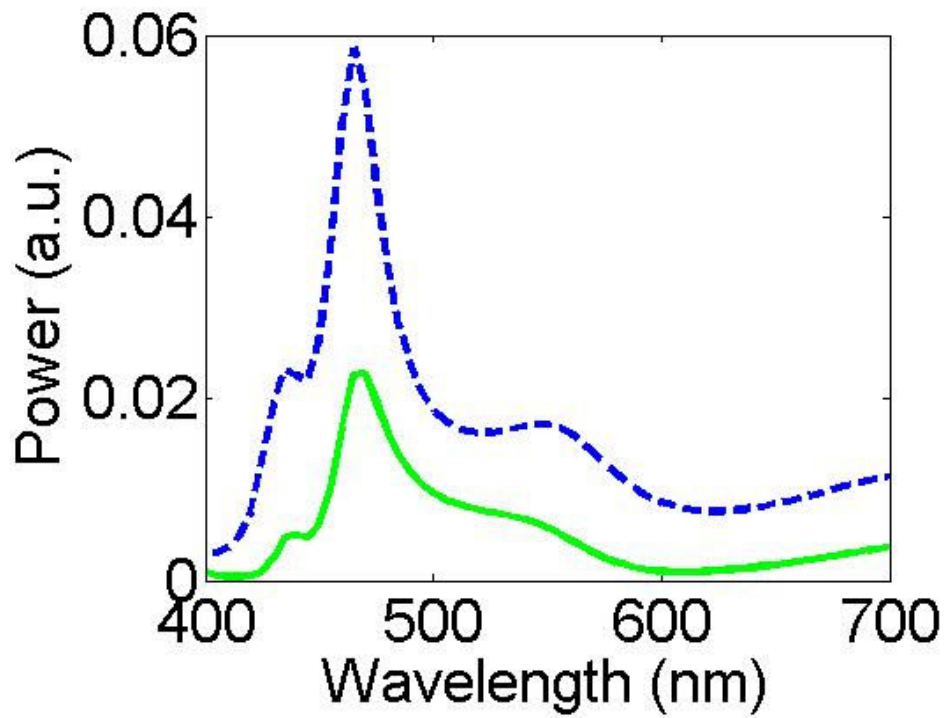
Fig. 4.13 Spectra of total emission (dashed curve) and downward emission (solid curve) for structure F.
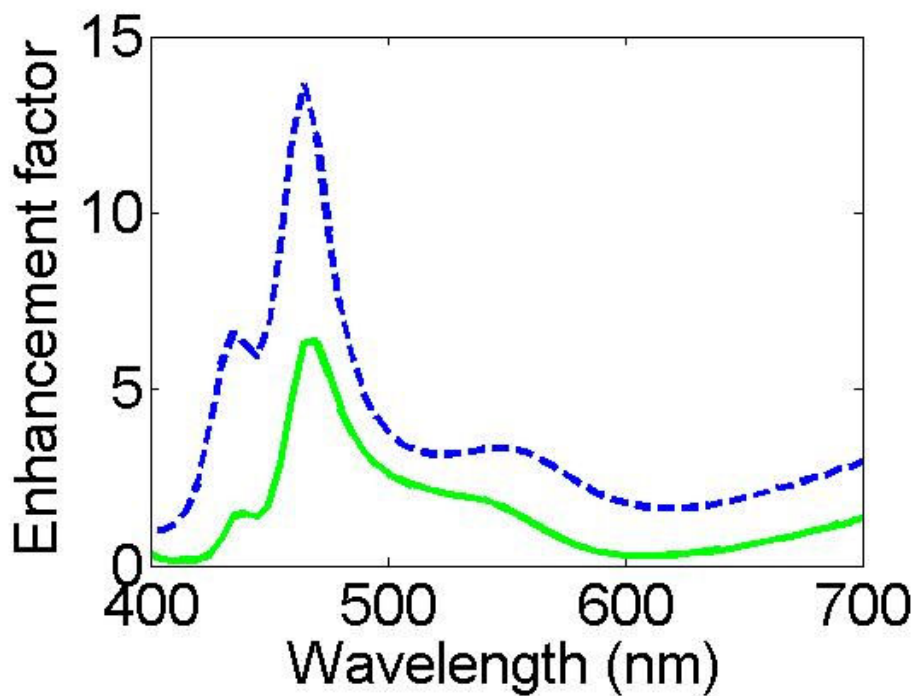
Fig. 4.14 Spectra of enhancement factor of total emission (dashed curve) and downward emission (solid curve) for structure F.
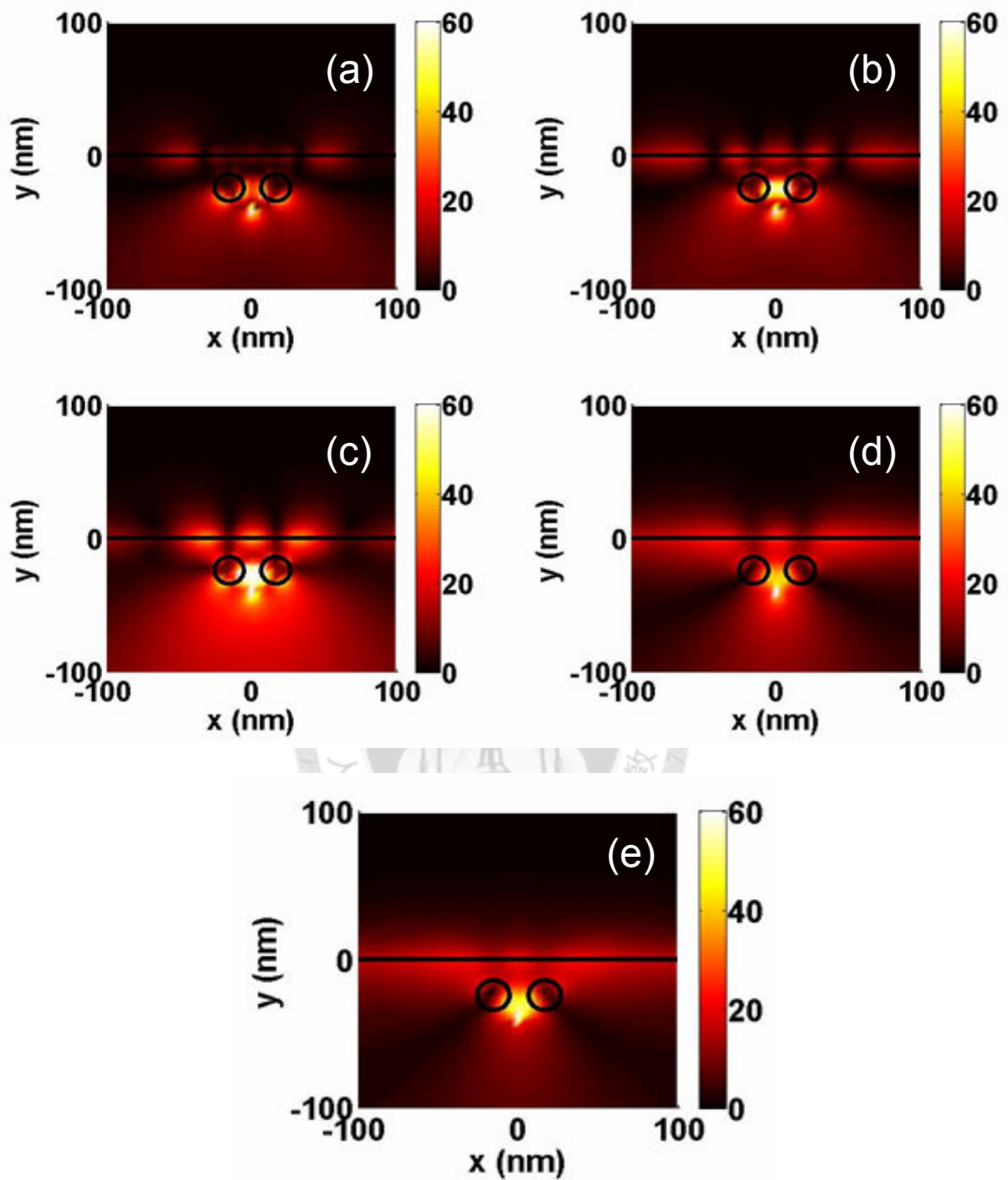
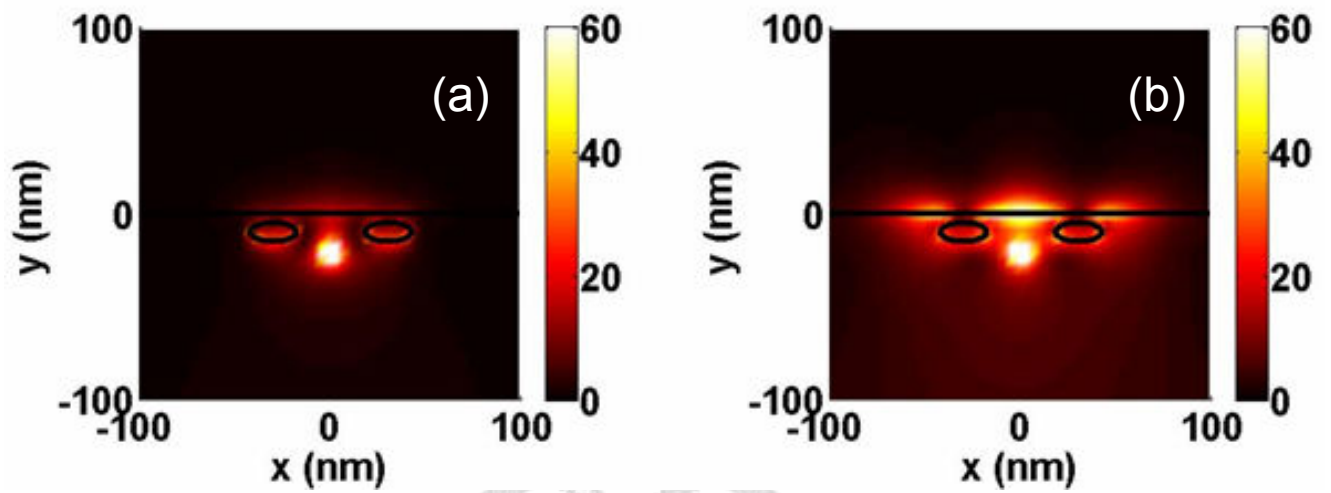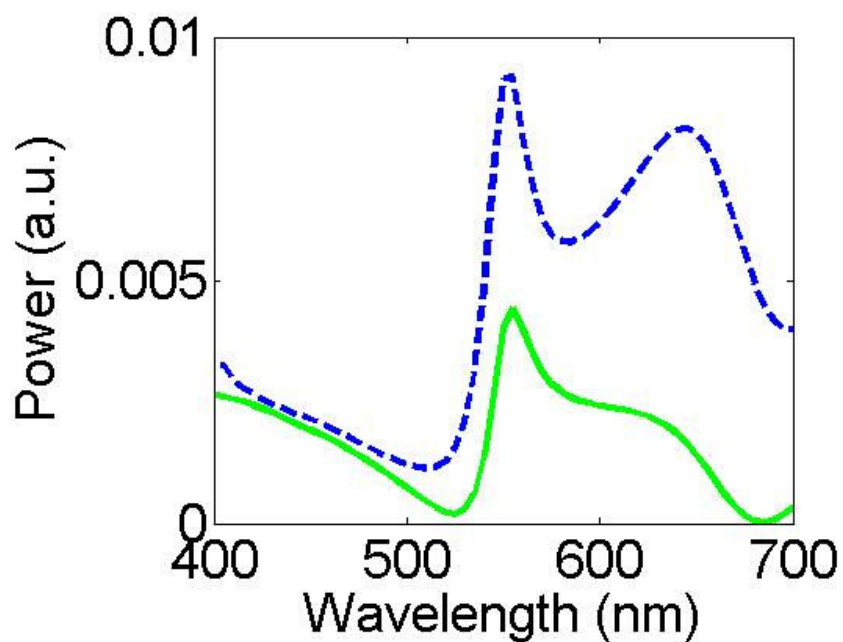Fig. 4.15 Distributions of the absolute values of magnetic field for structure F at wavelength 435 nm (a), 450 nm (b), 470 nm (c), 540 nm (d), and 570 nm (e).
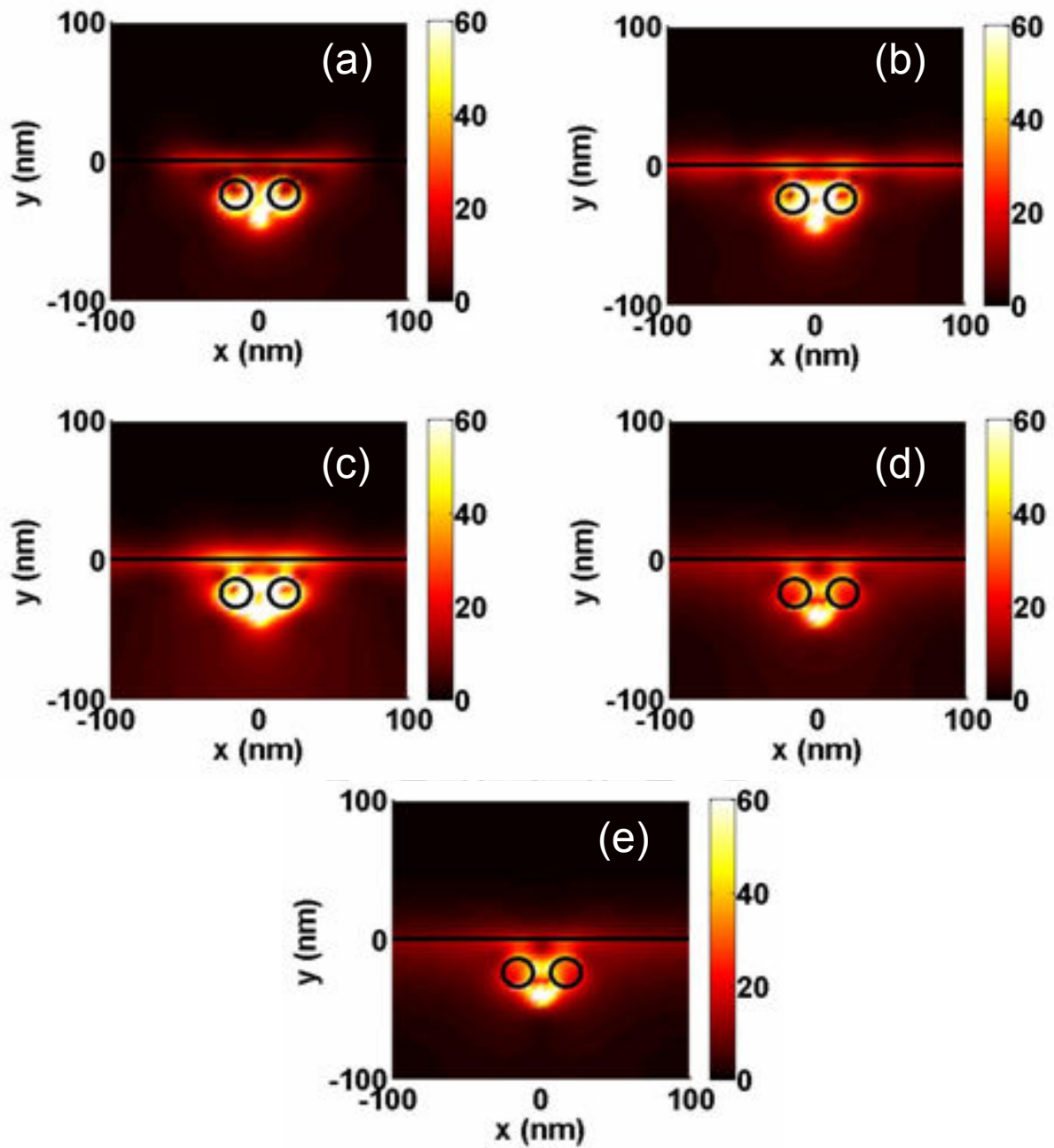
Fig. 4.16 Distributions of the absolute values of electric field for structure F at wavelength 435 nm (a), 450 nm (b), 470 nm (c), 540 nm (d), and 570 nm (e).
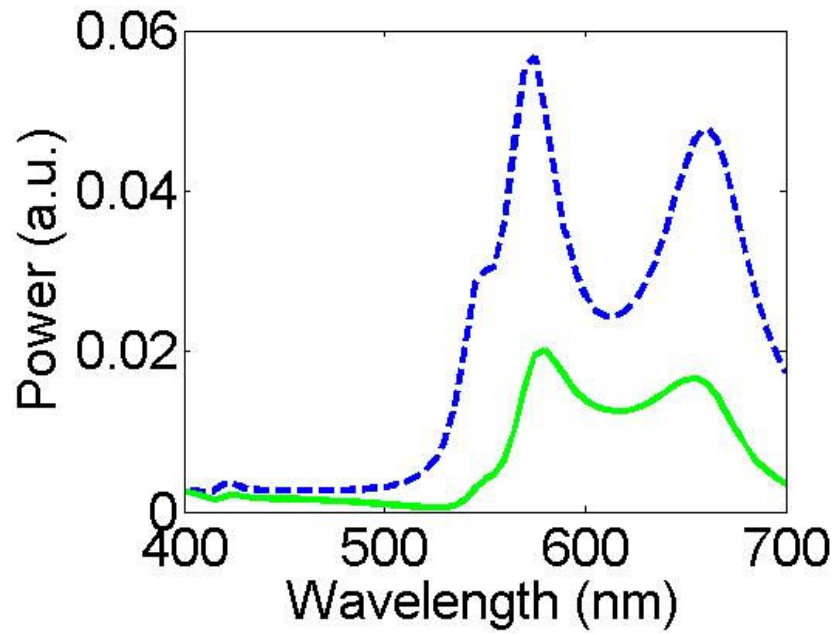
Fig. 4.17 Spectra of total emission (dashed curve) and downward

emission (solid curve) for structure G.
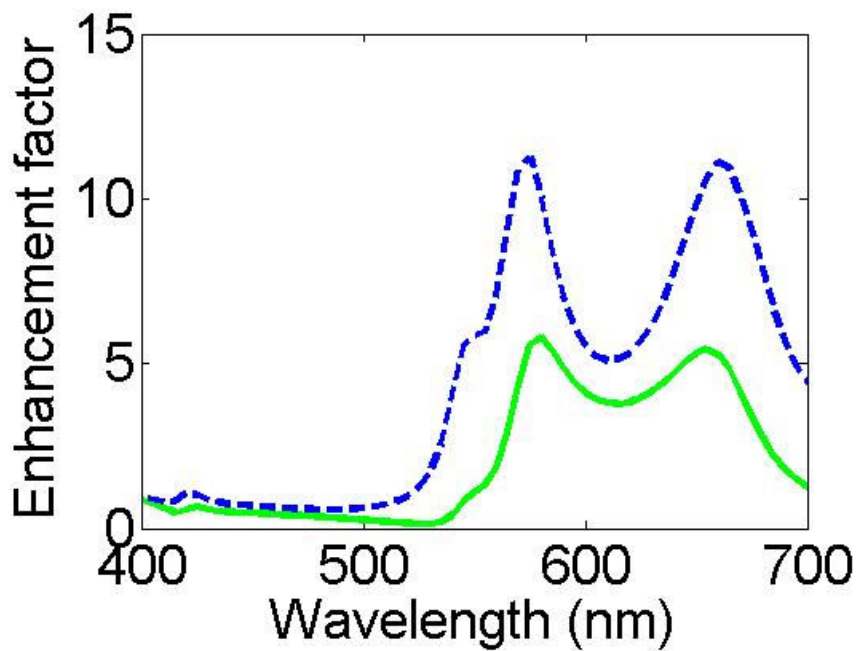
Fig. 4.18 Spectra of enhancement factor of total emission (dashed curve)

and downward emission (solid curve) for structure G.
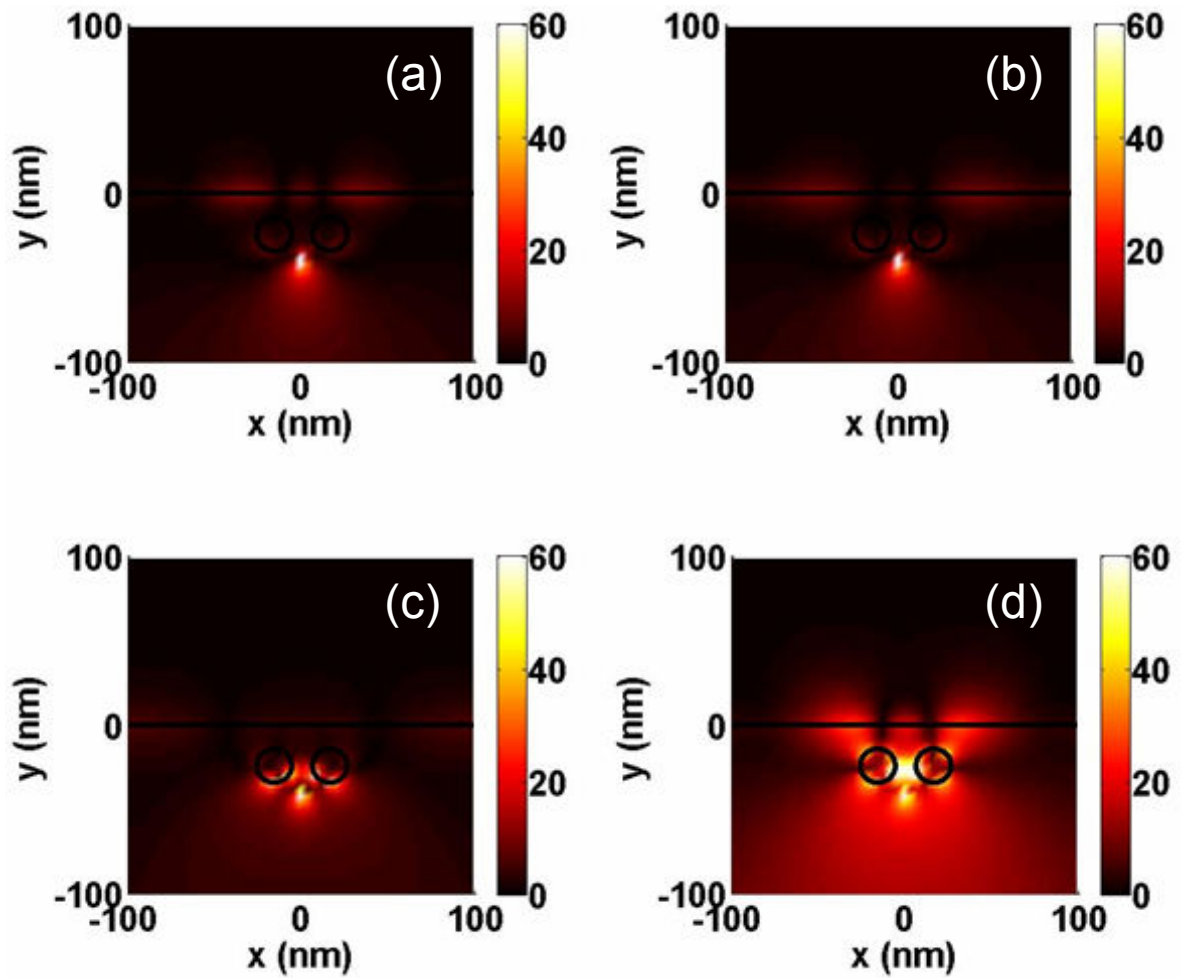
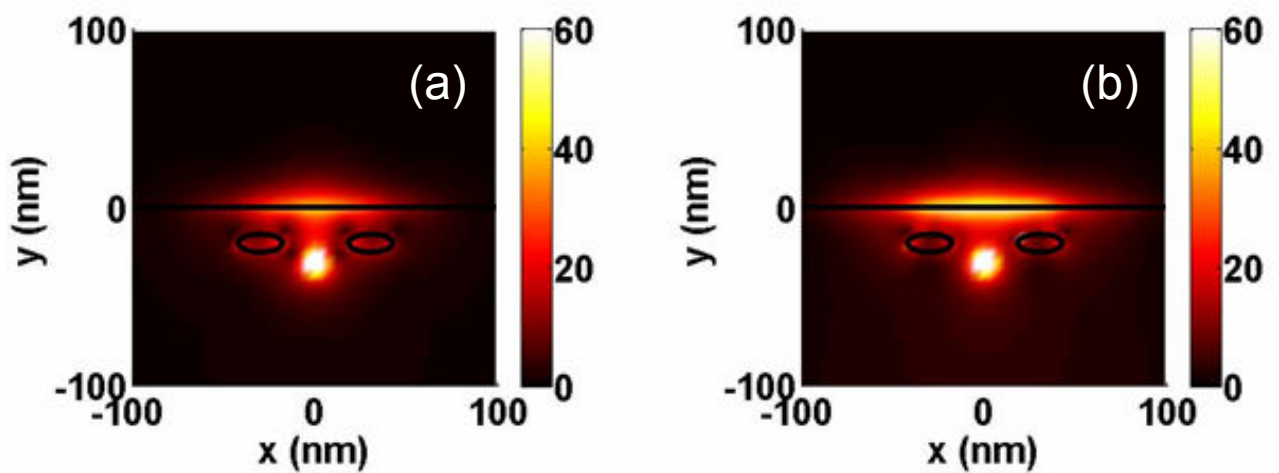Fig. 4.19 Distributions of the absolute values of magnetic field for structure G at wavelength 435 nm (a), 450 nm (b), 540 nm (c), and 570 nm (d).

Fig. 4.20 Distributions of the absolute values of electric field for structure

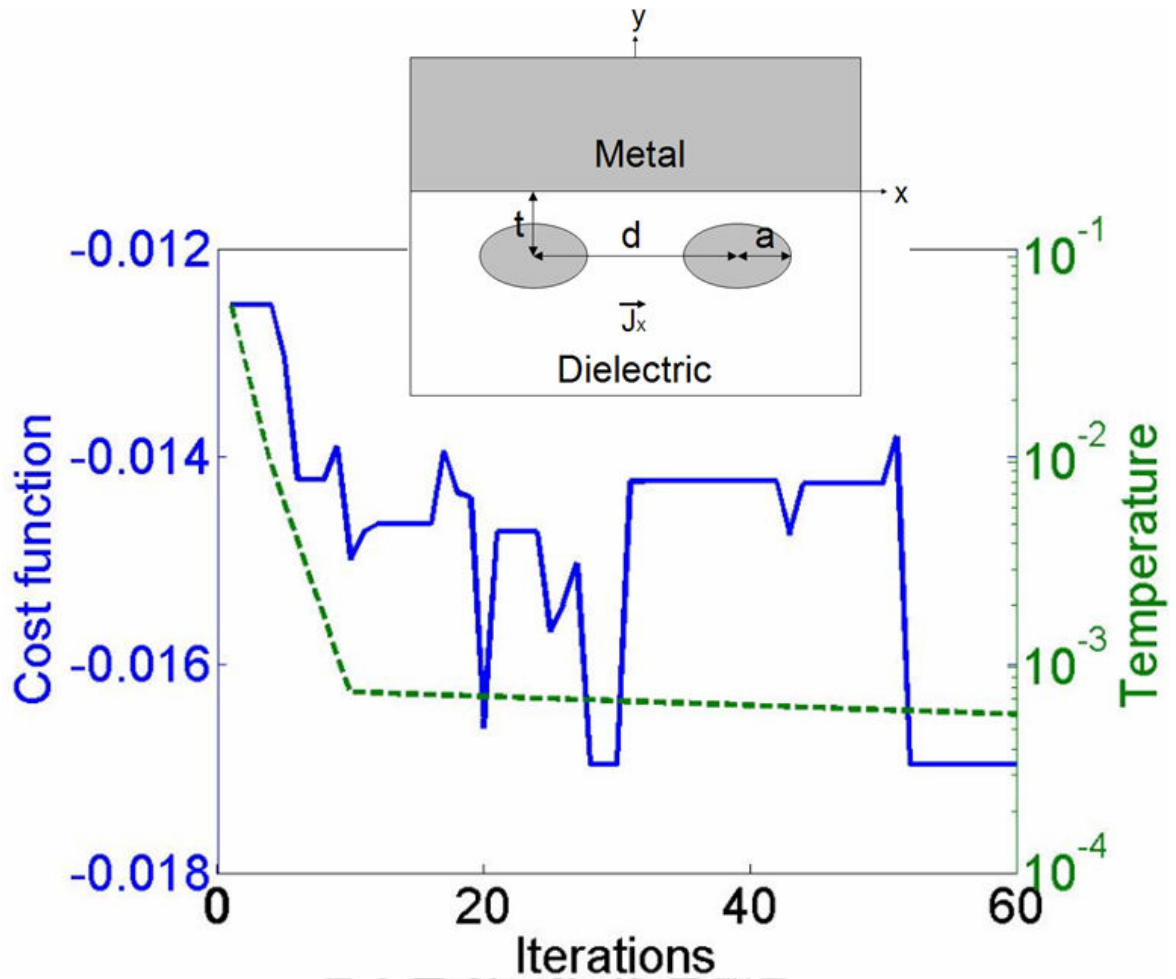G at wavelength 435 nm (a), 450 nm (b), 540 nm (c), and 570 nm (d).
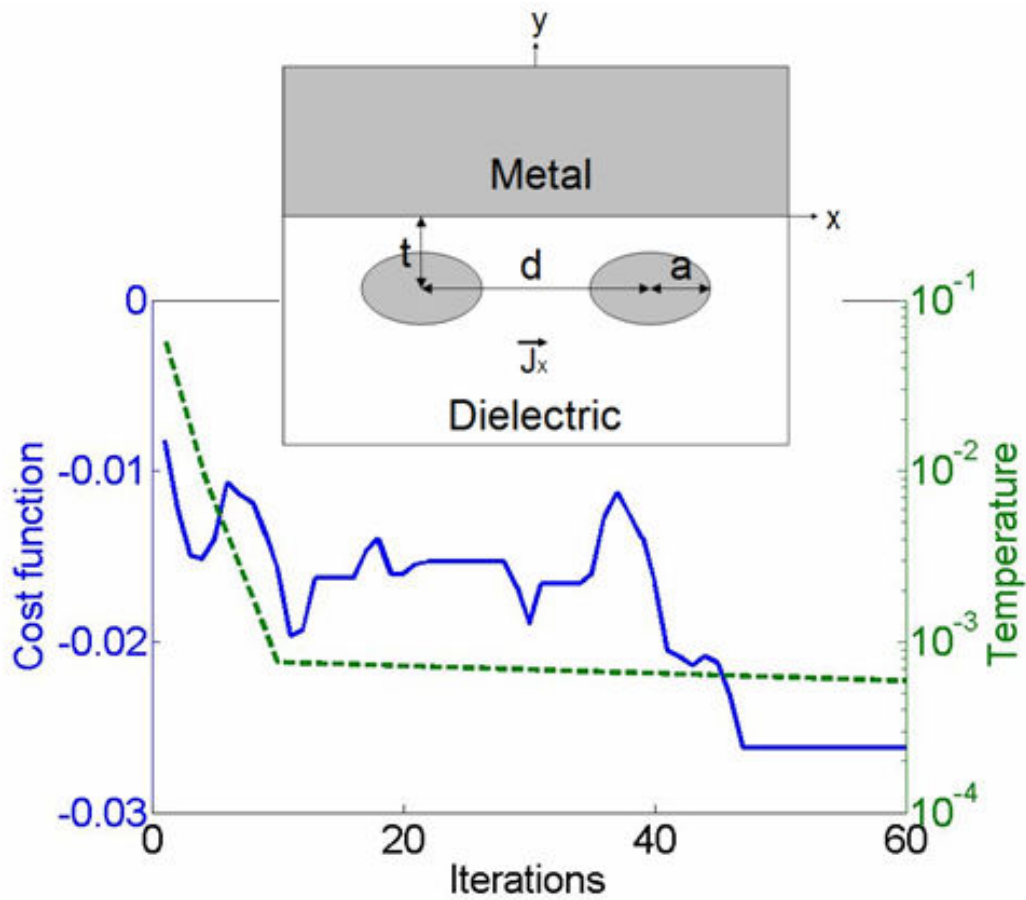
Fig. 4.21 Variation of cost function in the iteration process. The solid curve represents the cost function and the dashed curve represents the chosen temperature distribution used in the SA process. The synthetic structure is shown schematically in the insert. An x-oriented dipole, denoted by an arrow and labeled by J_x, is located at $(x, y) = (0, -h)$. The metal-dielectric flat interface is at $y = 0$.
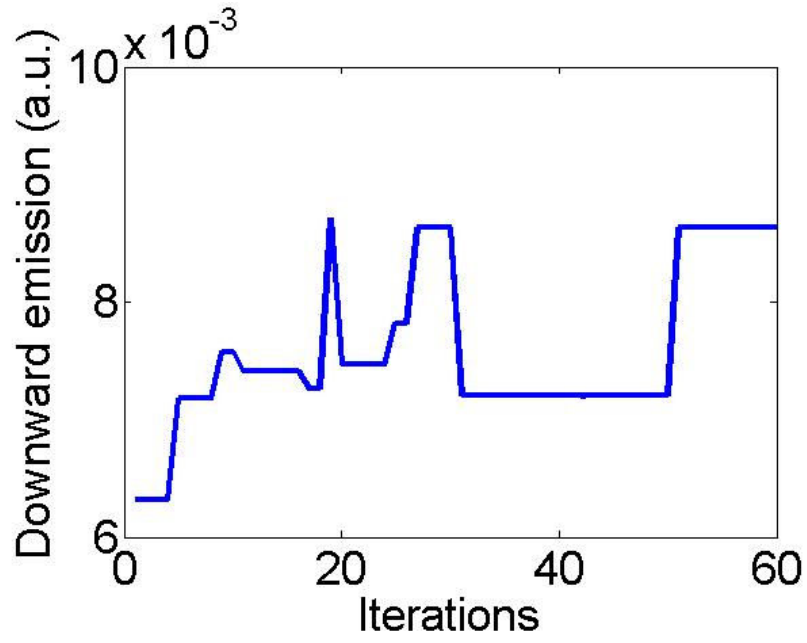
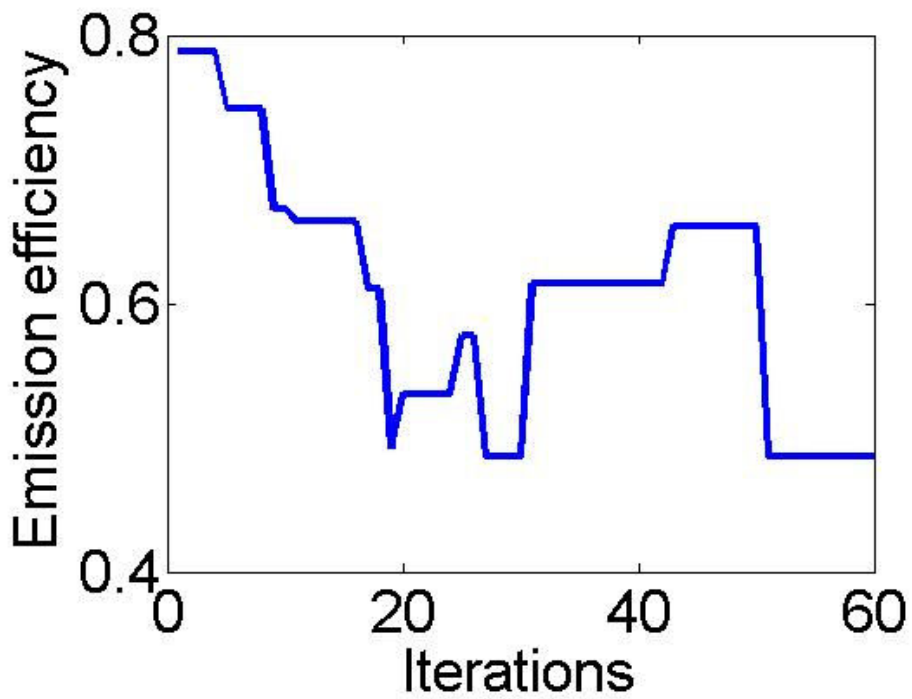Fig. 4.22 Variation of downward emission in the iteration process.
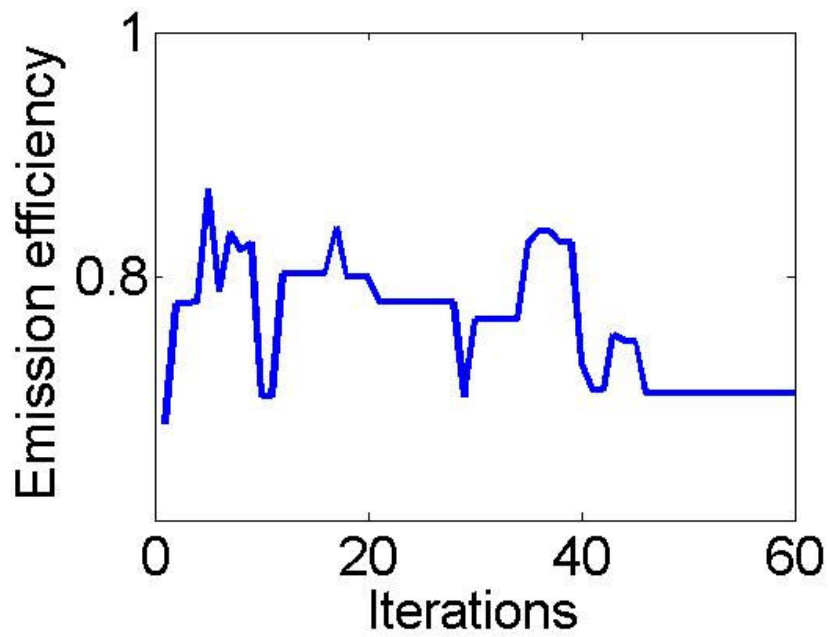
Fig. 4.23 Variation of emission efficiency in the iteration process.
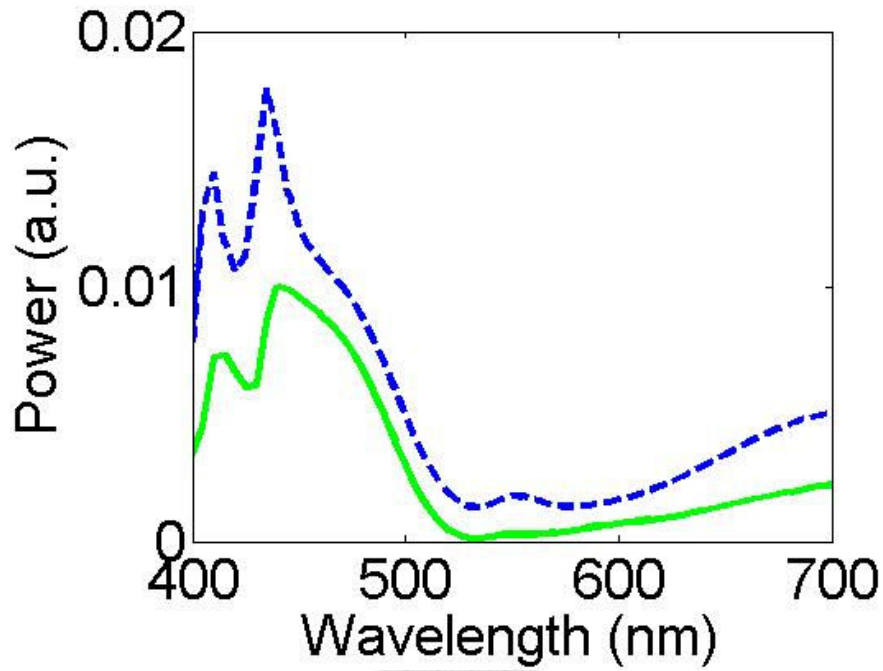
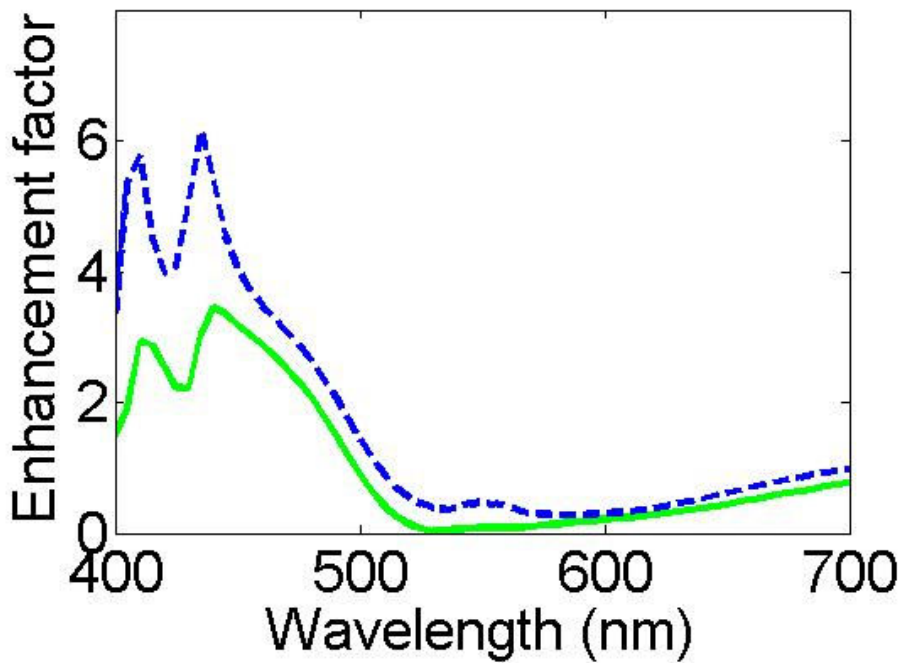Fig. 4.24 Spectra of total emission (dashed curve) and downward emission (solid curve) for structure H.

Fig. 4.25 Spectra of enhancement factor of total emission (dashed curve) and downward emission (solid curve) for structure H.

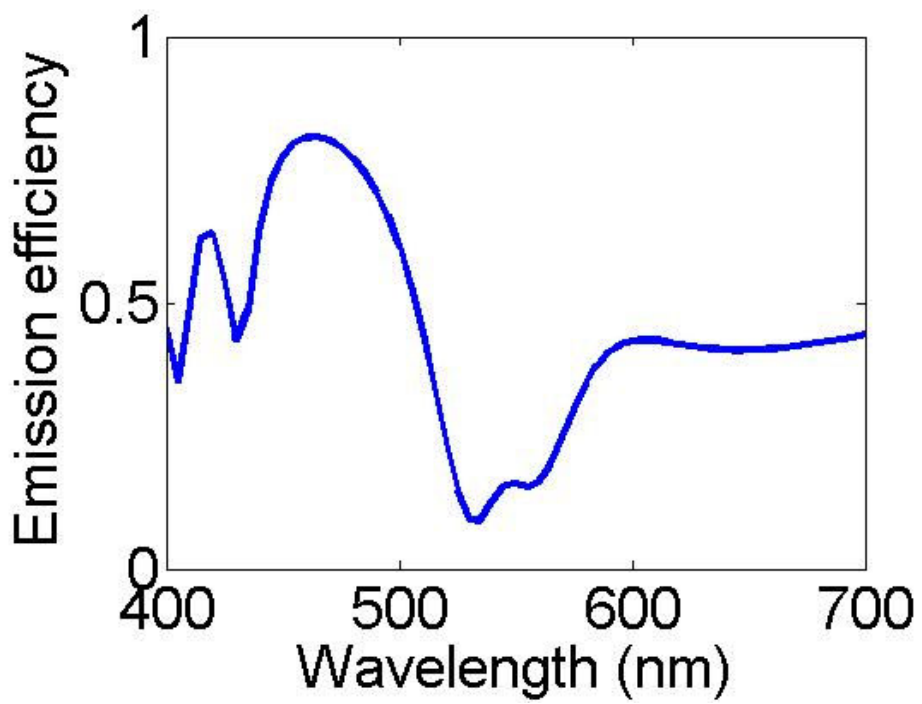Fig. 4.26 Spectrum of emission efficiency for structure H.
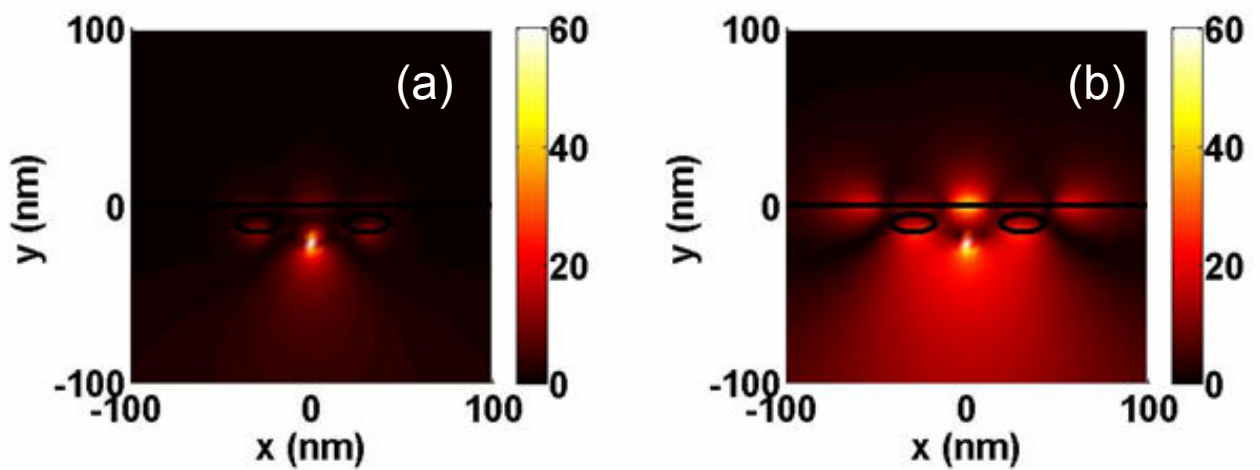
Fig. 4.27 Distributions of the absolute values of magnetic field for structure H at wavelength 435 nm (a) and 535 nm (b).

Fig. 4.28 Distributions of the absolute values of electric field for structure H at wavelength 435 nm (a) and 535 nm (b).

Fig. 4.29 Spectra of total emission (dashed curve) and downward emission (solid curve) for structure I.
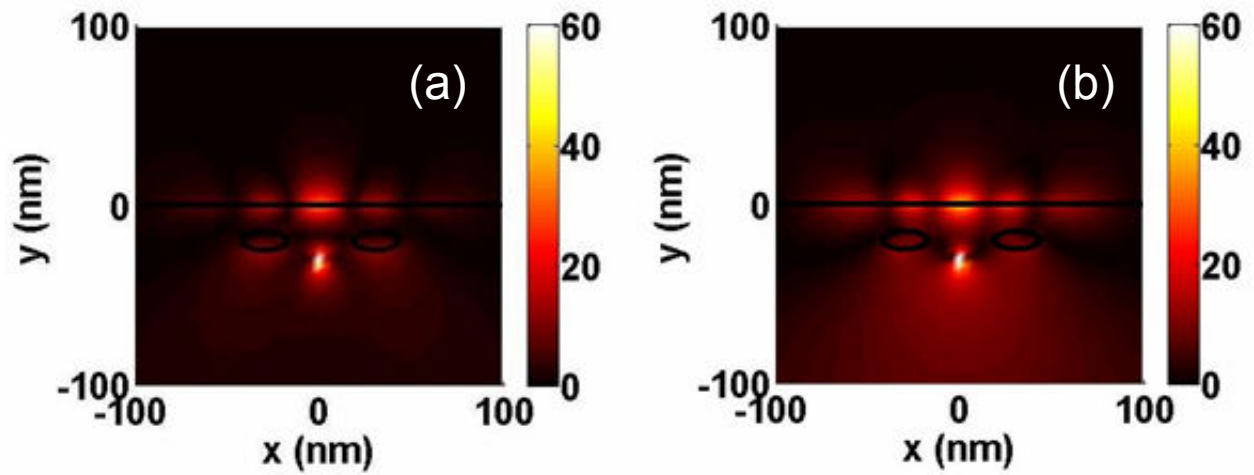
Fig. 4.30 Distributions of the absolute values of magnetic field for structure I at wavelength 535 nm (a) and 555 nm (b).

Fig. 4.31 Distributions of the absolute values of electric field for structure I at wavelength 535 nm (a) and 555 nm (b).

Fig. 4.32 Variation of cost function in the iteration process. The solid curve represents the cost function and the dashed curve represents the chosen temperature distribution used in the SA process. The synthetic structure is shown schematically in the insert. An x-oriented dipole, denoted by an arrow and labeled by J_x, is located at $(x, y) = (0, -h)$. The metal-dielectric flat interface is at $y = 0$.

Fig. 4.33 Variation of downward emission in the iteration process.

Fig. 4.34 Variation of emission efficiency in the iteration process.

Fig. 4.35 Spectra of total emission (dashed curve) and downward emission (solid curve) for structure J.

Fig. 4.36 Spectra of enhancement factor of total emission (dashed curve) and downward emission (solid curve) for structure J.

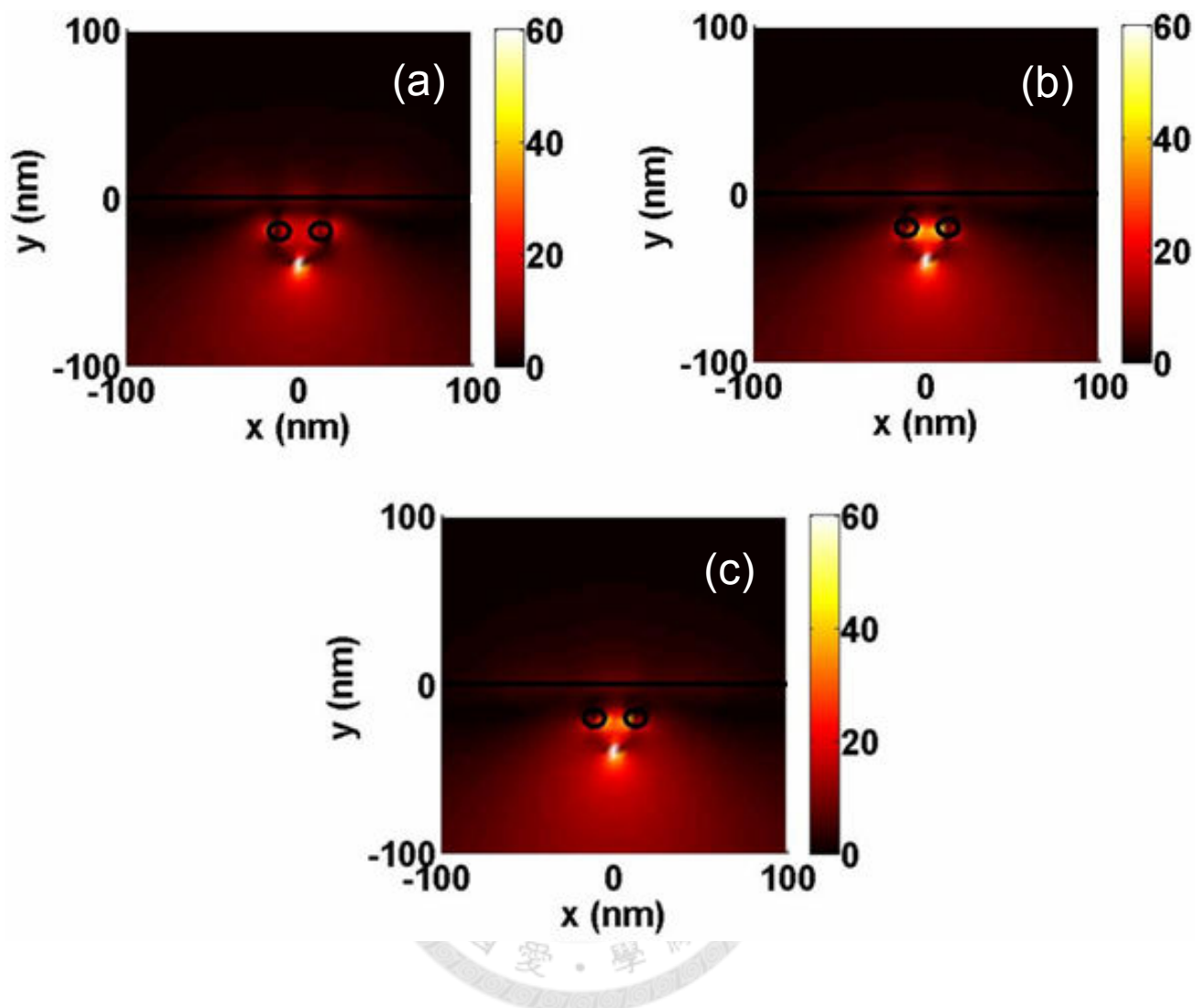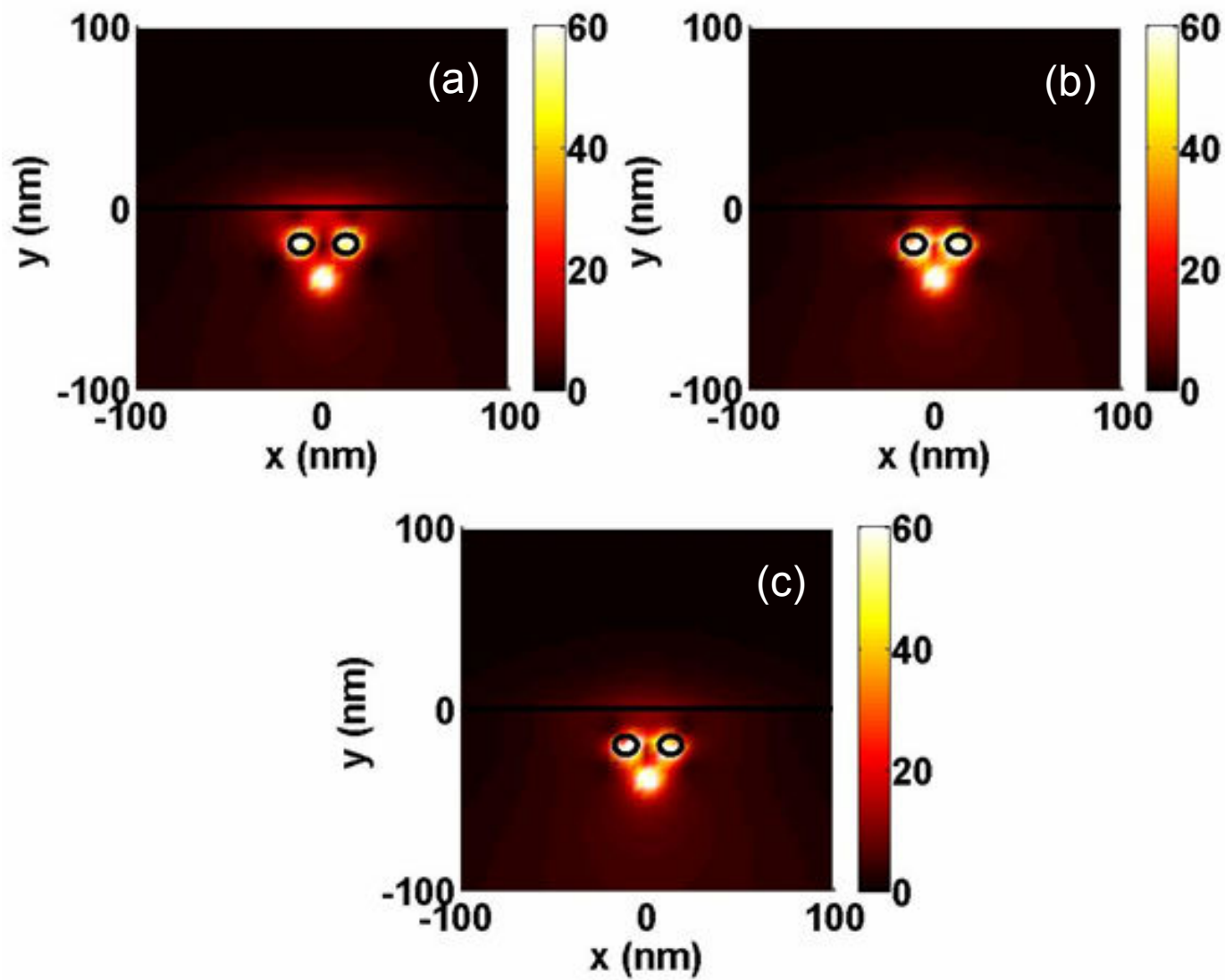Fig. 4.37 Spectrum of emission efficiency for structure J.

Fig. 4.38 Distributions of the absolute values of magnetic field for structure J at wavelength 415 nm (a), 435 nm (b), and 440 nm (c).

Fig. 4.39 Distributions of the absolute values of electric field for structure

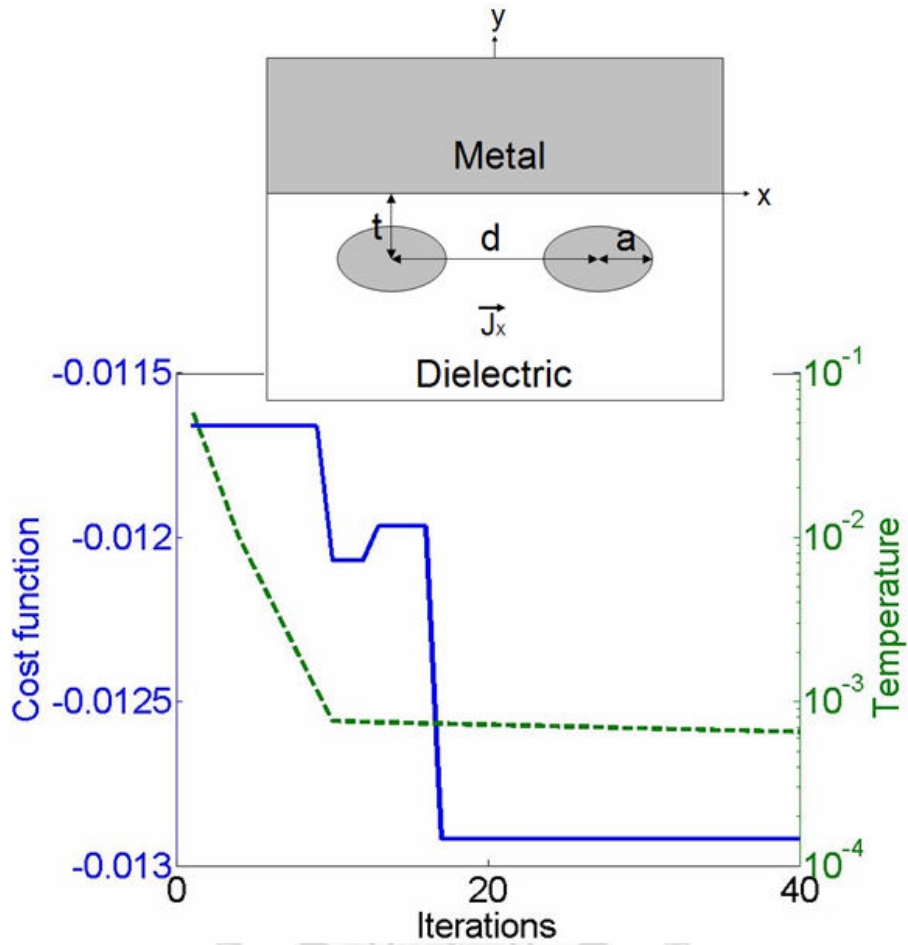J at wavelength 415 nm (a), 435 nm (b), and 440 nm (c).

Fig. 4.40 Variation of cost function in the iteration process. The solid curve represents the cost function and the dashed curve represents the chosen temperature distribution used in the SA process. The synthetic structure is shown schematically in the insert. An x-oriented dipole, denoted by an arrow and labeled by J_x, is located at $(x, y) = (0, -h)$. The metal-dielectric flat interface is at $y = 0$.
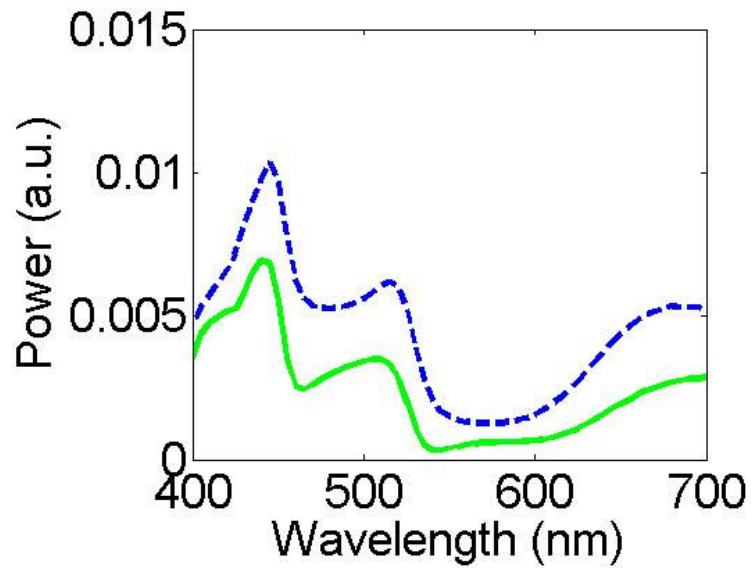
Fig. 4.41 Spectra of total emission (dashed curve) and downward emission (solid curve) for structure K.
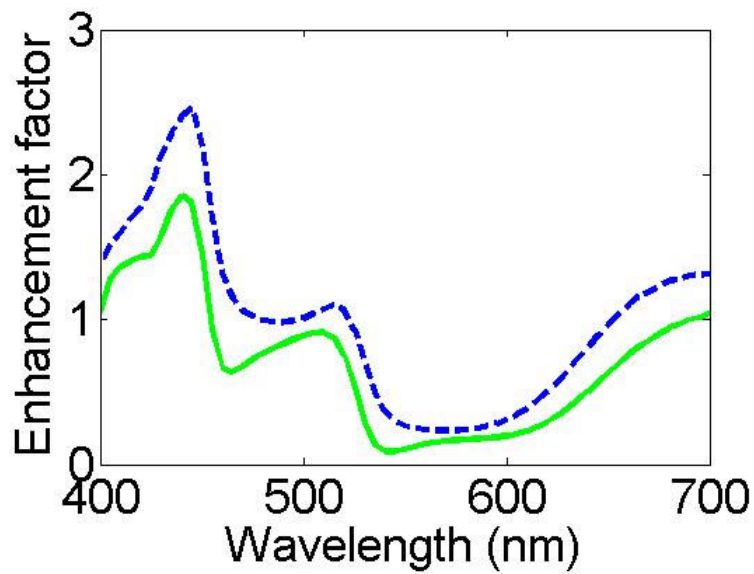

Fig. 4.42 Spectra of enhancement factor of total emission (dashed curve) and downward emission (solid curve) for structure K.
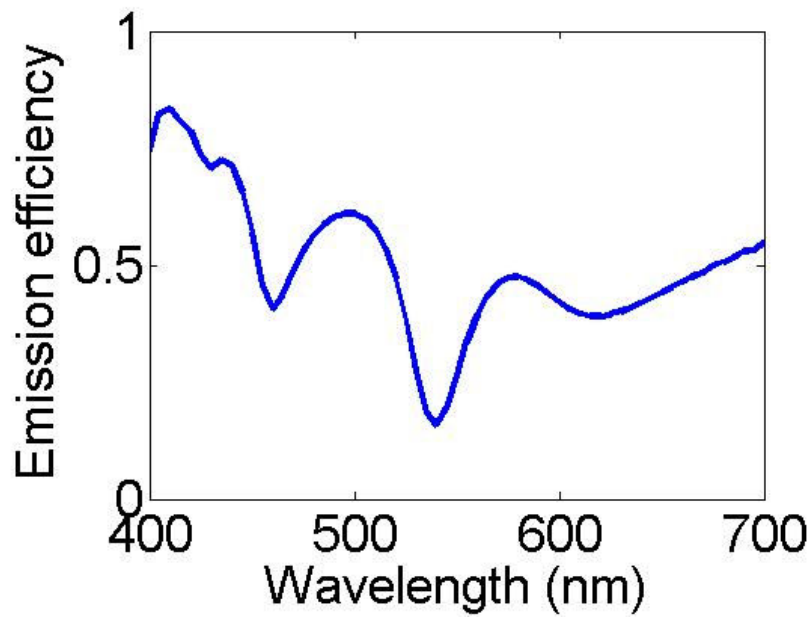
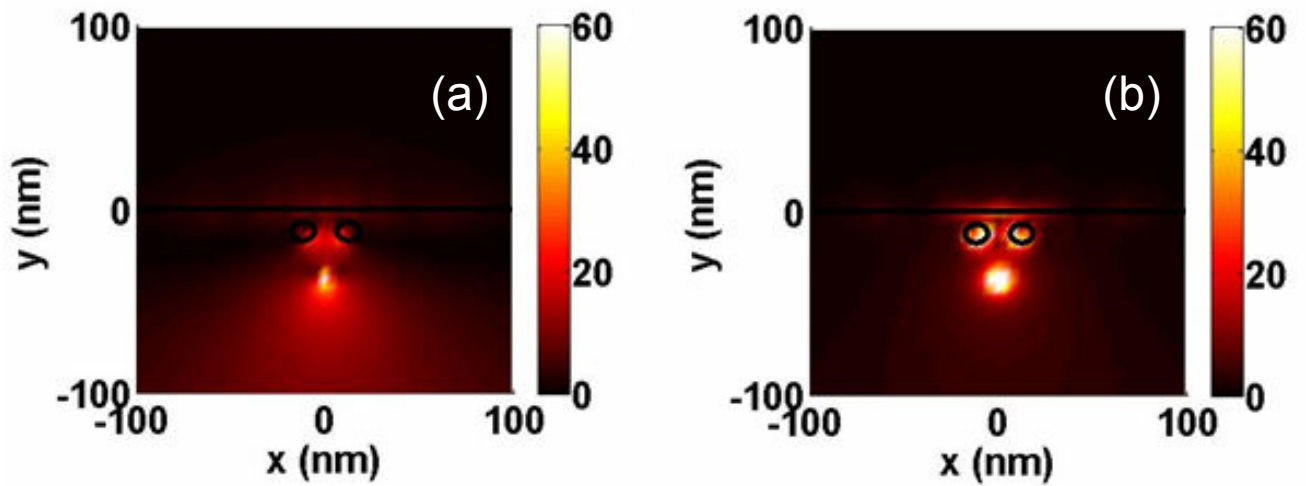Fig. 4.43 Spectrum of emission efficiency for structure K.

Fig. 4.44 Distributions of the absolute values of magnetic field (a) and

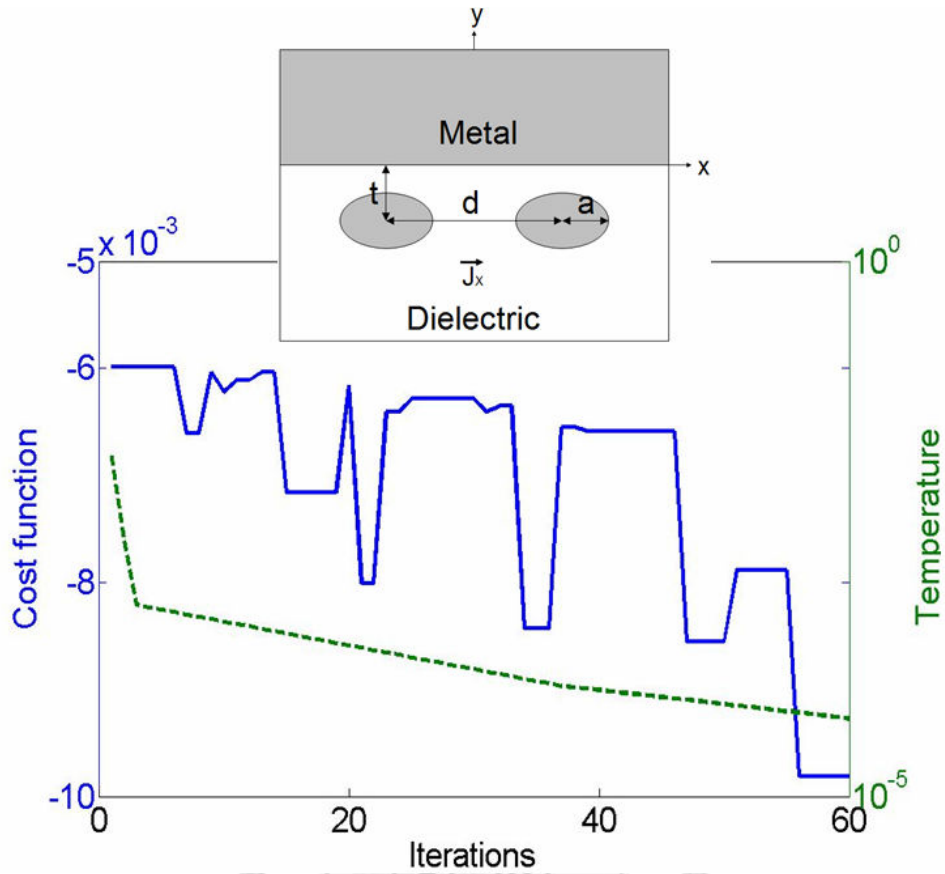electric field (b) for structure K at wavelength 435 nm.

Fig. 4.45 Variation of cost function in the iteration process. The solid curve represents the cost function and the dashed curve represents the chosen temperature distribution used in the SA process. The synthetic structure is shown schematically in the insert. An x-oriented dipole, denoted by an arrow and labeled by J_x, is located at $(x, y) = (0, -h)$. The metal-dielectric flat interface is at $y = 0$.
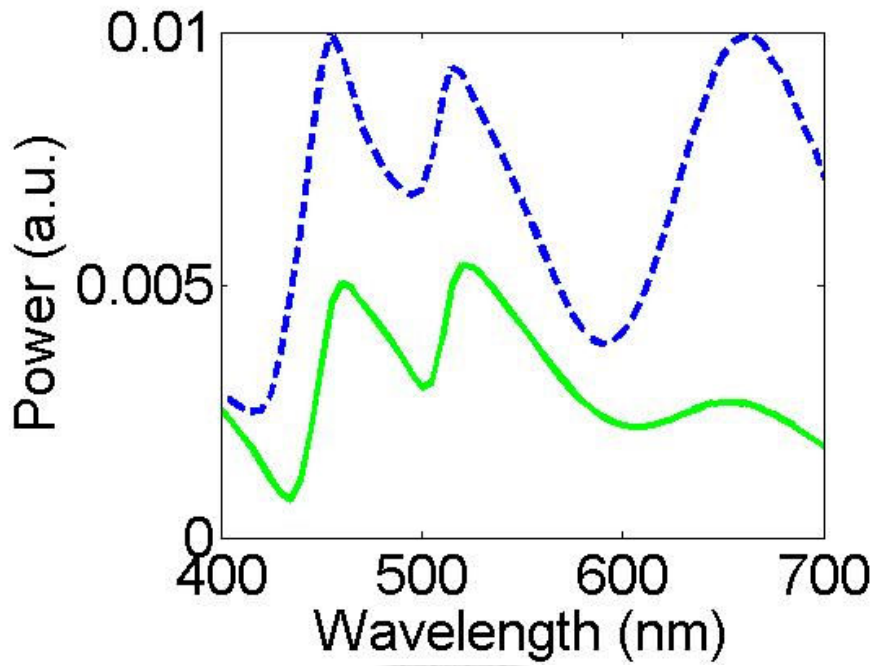
Fig. 4.46 Spectra of total emission (dashed curve) and downward emission (solid curve) for structure L.
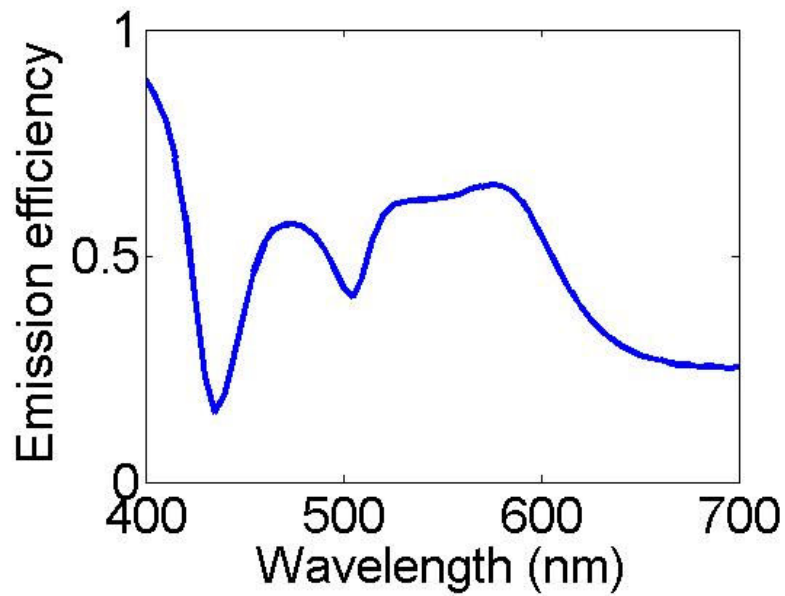

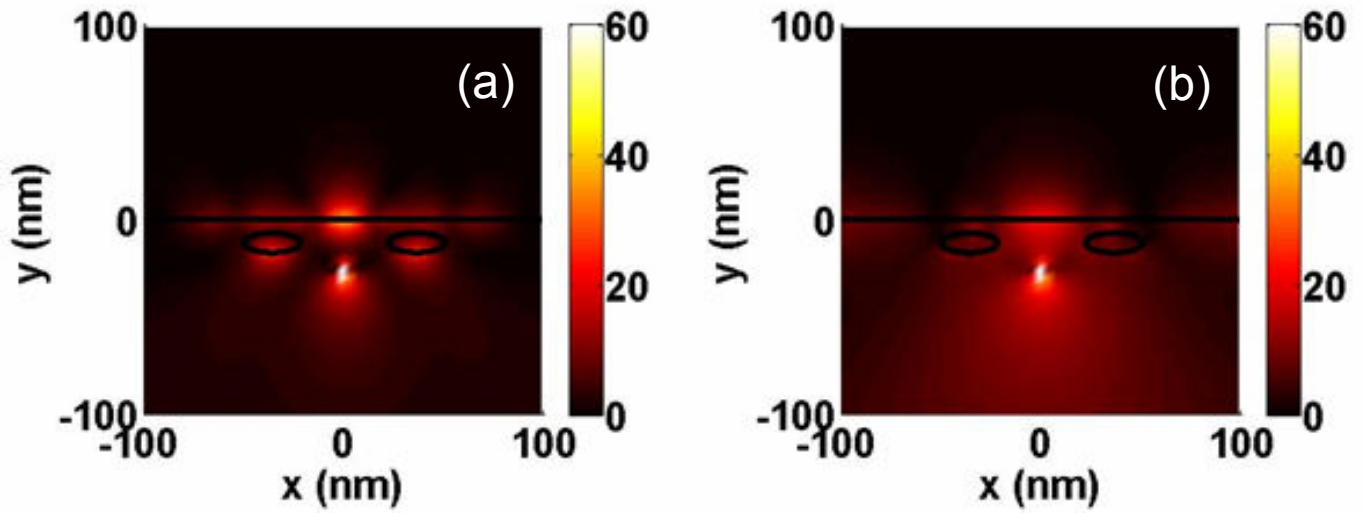Fig. 4.47 Spectrum of emission efficiency for structure L.

Fig 4.48 Distributions of the absolute values of magnetic field for structure L at wavelength 435 nm (a) and 535 nm (b).
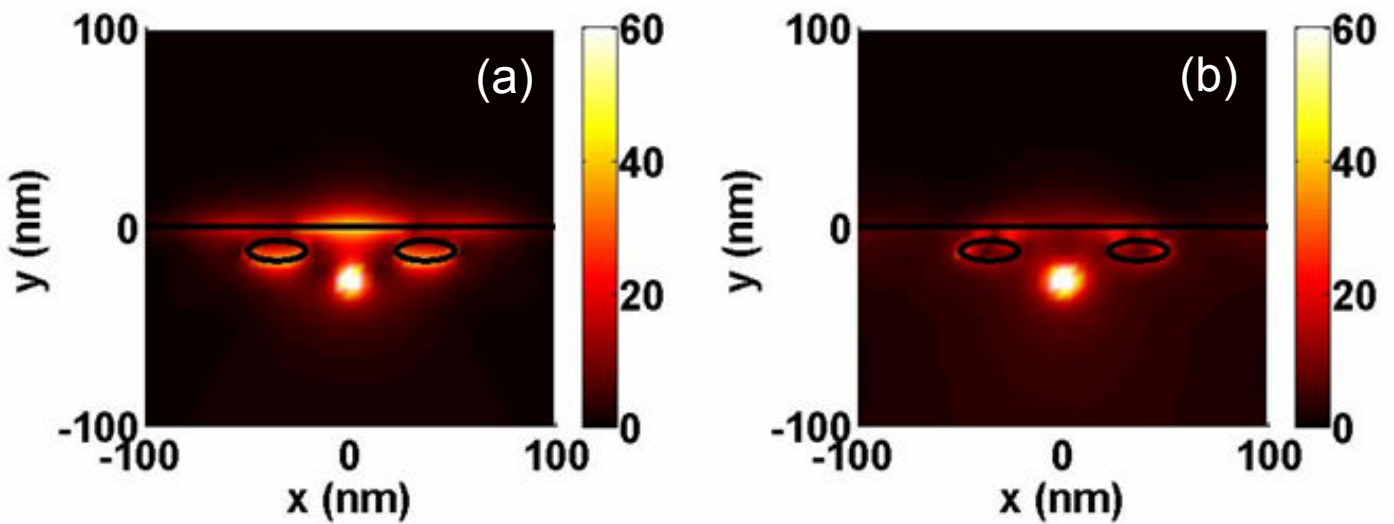

Fig. 4.49 Distributions of the absolute values of electric field for structure L at wavelength 435 nm (a) and 535 nm (b).

Fig. 4.50 Geometry of structure M.
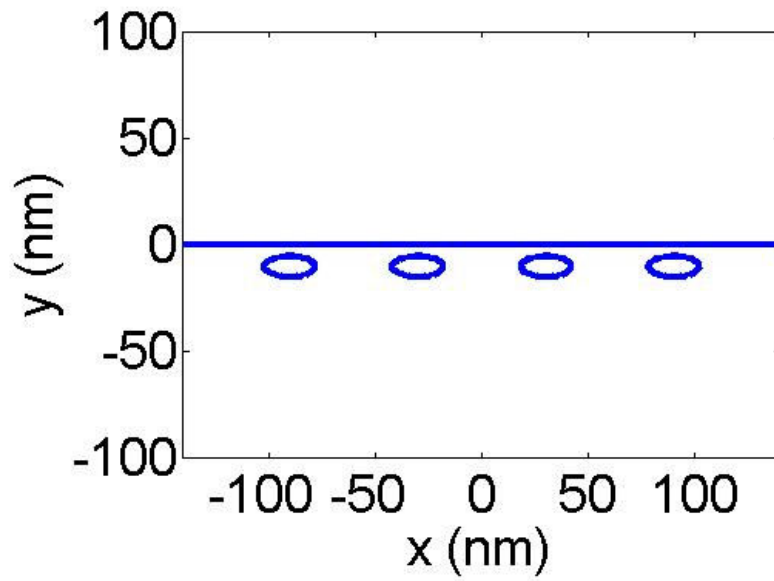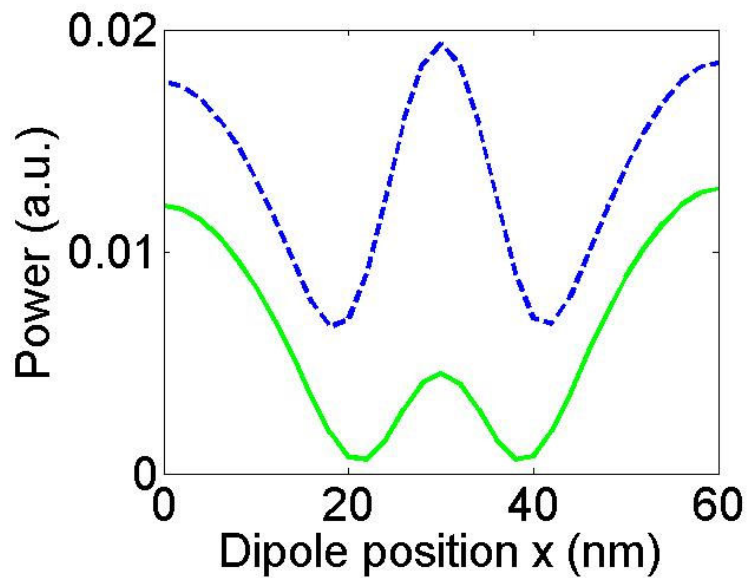

Fig. 4.51 Variations of total emission (dashed curve) and downward emission (solid curve) for structure M at wavelength 535 nm with the horizontal position of the dipole source.
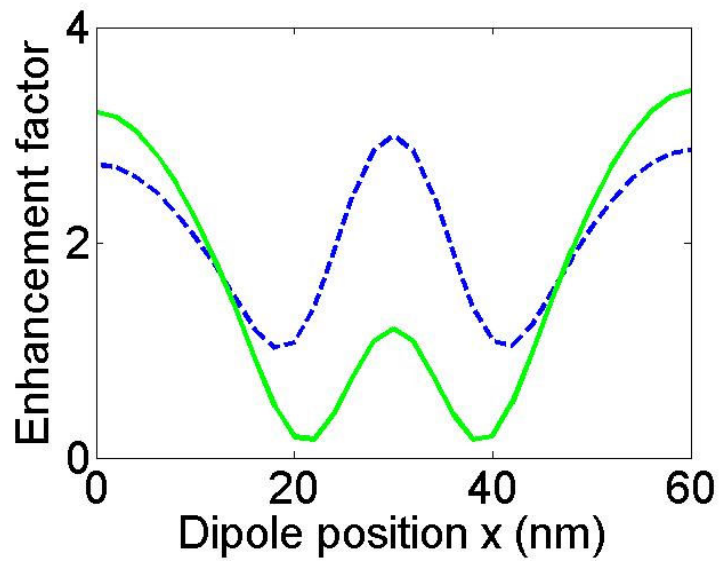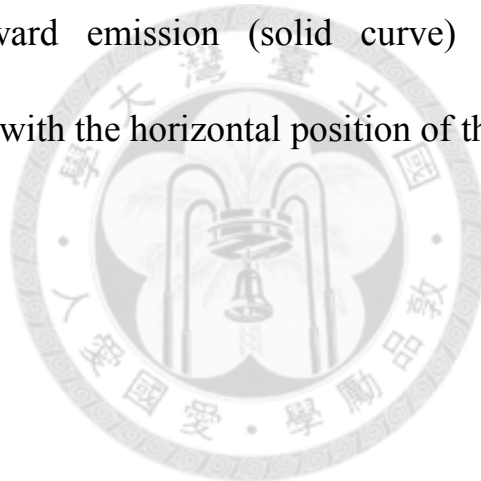
Fig. 4.52 Variations of enhancement factor of total emission (dashed curve) and downward emission (solid curve) for structure M at wavelength 535 nm with the horizontal position of the dipole source.

Chapter 5
Conclusions

In this thesis, we have succeeded in combining BIEM and SA to synthesize 2D metallic nanostructures with surface-plasmon resonance properties at designated wavelengths. The numerical results include three parts according to the possible applications: blue-light LEDs (wavelength 435 nm), white-light LEDs (wavelengths 450 nm and 570 nm), and green-light LEDs (wavelength 535 nm). For the blue-light LEDs, We have demostrated that the emission enhancement is best when both SPP and LSP are excited and coupled at a common resonant wavelength. It becomes worse when only one of SPP or LSP is effectively excited and hence the coupling between SPP and LSP is weak. The emission enhancement is worst when both SPP and LSP are weak. By using LSP resonances at different wavelengths, the structure (structure E) with emission enhancement simultaneously for yellow light and blue light has been investigated. This can provide a guideline to design the white-light LEDs. In the aspect of green-light LEDs, we have demonstrated that the downward emission and the emission efficiency can reach maxima

almost simultaneously when the SPP and LSP effectively couple at a common resonant wavelength. Through numerical simulations, it has been demonstrated that the coupling effect between SPP and LSP can indeed improve the emission performance of LEDs. Finally, for feasibility of fabrication, the variation of enhancement factor of either total emission or downward emission for structure M at wavelen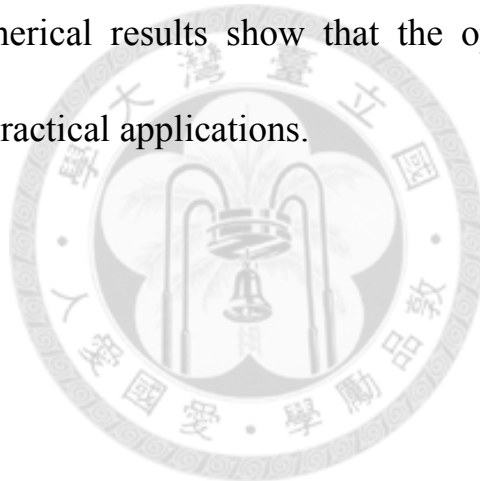gth 535 nm with the horizontal position of the dipole source has been investigated by simulation. Numerical results show that the optimal structures are indeed feasible for practical applications.

References

1. K. Okamoto, I. Niki, A. Shvartser, Y. Narukawa, T. Mukai, and A. Scherer, "Surface-plasmon-enhanced light emitters based on InGaN quantum wells," Nat. Mater., vol. 3, pp. 601-605, 2004.

2. K. Okamoto, I. Niki, A. Scherer, Y. Narukawa, T. Mukai, and Y.Kawakami, "Surface plasmon enhanced spontaneous emission rate of InGaN/GaN quantum wells probed by time-resolved photoluminescence spectroscopy," Appl. Phys. Lett., vol. 87, p. 071102, 2005.

3. K. Okamoto, I. Niki, A. Shvartser, G. Maltezos, Y. Narukawa, T. Mukai, Y. Kawakami, and A. Scherer, "Surface plasmon enhanced bright light emission from InGaN/GaN," Phys. Stat. Sol., vol. 204, pp. 2103-2107, 2007.

4. C. Y. Chen, Y. C. Lu, D. M. Yeh, and C. C. Yang, "Influence of the quantum-confined Stark effect in an InGaN/GaN quantum well on its coupling with surface plasmon for light emission enhancement," Appl. Phys. Lett., vol. 90, p. 183114, 2007.

5. Y. C. Lu, C. Y. Chen, D. M. Yeh, C. F. Huang, T. Y. Tang, J. J. Huang, and C. C. Yang, "Temperature dependence of the surface plasmon coupling with an InGaN/GaN quantum well," Appl. Phys. Lett., vol. 90, p. 193103, 2007.

6. D. M. Yeh, C. F. Huang, Y. C. Lu, C. Y. Chen, T. Y. Tang, J. J. Huang, K. C. Shen, Y. J. Yang, and C. C. Yang, "Surface plasmon leakage in its coupling with an InGaN/GaN quantum well through an Ohmic contact," Appl. Phys. Lett., vol. 91, p. 063121, 2007.

7. D. M. Yeh, C. F. Huang, C. Y. Chen, Y. C. Lu, and C. C. Yang, "Surface plasmon coupling effect in an InGaN/GaN

single-quantum-well light-emitting diode," Appl. Phys. Lett., vol. 91, p. 171103, 2007.

8. D. M. Yeh, C. Y. Chen, Y. C. Lu, C. F. Huang, and C. C. Yang, "Formation of various metal nanostructures with thermal annealing to control the effective coupling energy between a surface plasmon and an InGaN/GaN quantum well," Nanotechnology, vol. 18, p. 265402, 2007.

9. G. Sun, J. B. Khurgin, and R. A. Soref, "Practicable enhancement of spontaneous emission using surface plasmons," Appl. Phys. Lett., vol. 90, p. 111107, 2007.

10. J. B. Khurgin, G. Sun, and R. A. Soref, "Enhancement of luminescence efficiency using surface plasmon polaritons: figures of merit," J. Opt. Soc. Am. B, vol. 24, pp. 1968-1980, 2007.

11. I. Gontijo, M. Boroditsky, and E. Yablonovitch, "Coupling of InGaN quantum-well photoluminescence to silver surface plasmons," Phys. Rev. B, vol. 60, pp. 11564-11567, 1999.

12. R. Paiella, "Tunable surface plasmons in coupled metallo-dielectric multiple layers for light-emission efficiency enhancement," Appl. Phys. Lett., vol. 87, p. 111104, 2005.

13. D. Lepage and J. J. Dubowski, "Surface plasmon assisted photoluminescence in GaAs-AlGaAs quantum well microstructures," Appl. Phys. Lett., vol. 91, p. 163106, 2007.

14. J. Chen, N. H. Shen, C. Cheng, Y. X. Fan, J. Ding, and H. T. Wang, "Tunable resonance in surface-plasmon-polarition enhanced spontaneous emission using a denser dielectric cladding," Appl. Phys. Lett., vol. 89, p. 051916, 2006.

15. D. Crouse, "Numerical modeling and electromagnetic resonant modes in complex grating structures and optoelectronic device applications," IEEE Transactions on Electron Devices, vol. 52, pp.

2365-2373, 2005.

16. D. Crouse and P. Keshavareddy, "Role of optical and surface plasmon modes in enhanced transmission and applications," Opt. Express, vol. 13, pp. 7760-7771, 2005.

17. Wei-Chih Liu and Din Ping Tsai, "Optical tunneling effect of surface plasmon polaritons and localized surface plasmon resonance," Phys. Rev. B, vol. 65, p. 155423, 2002.

18. J. Y. Wang, Y. W. Kiang, and C. C. Yang, "Emission enhancement behaviors in the coupling between surface plasmon polariton on a one-dimensional metallic grating and a light emitter," Appl. Phys. Lett., vol. 91, p. 233104, 2007.

19. J. P. Dowling and C. M. Bowden, "Atomic emission rates in inhomogeneous-media with applications to photonic band structures," Phys. Rev. A, vol. 46, pp. 612-622, 1992.

20. S. Kirkpatrick, C. D. Gelatt, Jr., and M. P. Vecchi, "Optimization by simulated annealing," Science, vol. 220, pp. 671-680, 1983.

21. N. Metropolis, A. Rosenbluth, M. Rosenbluth, A. Teller, and E. Teller, "Equation of state calculations by fast computing machines," J. Chem. Phys. vol. 21, pp. 1087-1092, 1953.

22. F. Wooten, *Optical Properties of Solids*, New York: Academic Press, 1972.

23. S. A. Maier, *Plasmonics*, New York: Springer, 2007.

24. R. E. Plonsey and R. E. Collin, *Principles and Applications of Electromagnetic Fields*, New York: McGraw-Hill, 1961.

25. J. A. Kong, *Electromagnetic Wave Theory*, New York: John Wiley & Sons, 1986.

26. C. F. Bohren and D. R. Huffman, *Absorption and Scattering of Light by Small Particles*, New York: John Wiley & Sons, 1983.

27. A. Neogi, C. W. Lee, H. O. Everitt, T. Kuroda, A. Tackeuchi, and E. Yablonovitch, "Enhancement of spontaneous recombination rate in a quantum well by resonant surface plasmon coupling," Phys. Rev. B, vol. 66, p. 153305, 2002.

28. A. Yariv, *Quantum Electronics*, New York: John Wiley & Sons, 1989.

29. K. Yashiro and S. Ohkawa, "Boundary element method for electromagnetic scattering from cylinders," IEEE Trans. Antennas Propagat., vol. 33, pp. 383-389, 1985.

30. L. C. Trintinalia and H. Ling, "Integral equation modeling of multilayered doubly-periodic lossy structures using periodic boundary condition and a connection scheme," IEEE Trans. Antennas Propagat., vol. 52, pp. 2253-2261, 2004.

31. T. Sondergaard, S. I. Bozhevolnyi, and A. Boltasseva, "Theoretical analysis of ridge grating for long-range surface plasmon polaritons," Phys. Rev. B, vol. 73, p. 045320, 2006.

32. C. A. Balanis, *Advanced Engineering Electromagnetics*, New York: John Wiley & Sons, 1989.

33. K. M. Chen, "A mathematical formulation of the equivalence principle," IEEE Trans. Microwave Theory Tech, vol. 37, pp. 1576-1581, 1989.

34. J. A. Stratton, *Electromagnetic Theory*, New York: McGraw-Hill, 1941.

35. J. Y. Wang, C. C. Yang, and Y. W. Kiang, "Numerical study on surface plasmon polariton behaviors in periodic metal-dielectric structures using a plane-wave-assisted boundary integral-equation method ," Opt. Express, vol. 15, pp. 9048-9062, 2007.

36. 呂辰陽，“無螢光體雙波長白光 LED,” 全亞文化 Asia-info –
ET 電子技術雜誌, 264 期, 2008.